Structural dynamics underlying gating and regulation in IP_3R channel

Guizhen Fan[1]*, Mariah R. Baker[1]*, Lara E. Terry[2], Vikas Arige[2], Muyuan Chen[3], Alexander B. Seryshev[1], Matthew L. Baker[1], Steven J. Ludtke[3], David I. Yule[2+] & Irina I. Serysheva[1+]

[1]Department of Biochemistry and Molecular Biology, Structural Biology Imaging Center, McGovern Medical School at The University of Texas Health Science Center at Houston, 6431 Fannin Street, Houston, TX 77030, USA;
[2]Department of Pharmacology and Physiology, School of Medicine and Dentistry, University of Rochester, Rochester, New York 14642
[3]Verna and Marrs McLean Department of Biochemistry and Molecular Biology, Baylor College of Medicine, One Baylor Plaza, Houston, TX 77030, USA.

*These authors contributed equally to this work
[+]Correspondence

ABSTRACT

Inositol-1,4,5-trisphosphate receptors (IP_3Rs) are activated by IP_3 and Ca^{2+} and their gating is regulated by various intracellular messengers that finely tune the channel activity. Here, using single particle cryo-EM analysis we determined 3D structures of the nanodisc-reconstituted IP_3R1 channel in two ligand-bound states. These structures provide unprecedented details governing binding of IP_3, Ca^{2+} and ATP in IP_3R1, revealing conformational changes that couple ligand-binding to channel opening. Using a deep learning approach, we extracted dynamic properties of the key protein domains. From this, we find that IP_3 binding relies upon intrinsic flexibility of the cytoplasmic ARM2 domain. Our results highlight a key role of dynamic side chains surrounding the ion conduction path in regulating gating behavior of IP_3R channels. Altogether, this work defines a structural platform for mechanistic understanding of the molecular dynamics underlying ligand-binding, activation and regulation of the IP_3R activity.

INTRODUCTION

Inositol-1,4,5-trisphosphate receptors (IP_3Rs) are ubiquitous Ca^{2+} channels predominantly localized to the endoplasmic reticulum (ER) membranes. IP_3Rs play fundamental roles in the physiology of a diverse array of organisms as they mediate the release of Ca^{2+} from ER Ca^{2+} stores in response to diverse physiological stimuli. Decades of studies have revealed the central role that IP_3Rs have in generating complex intracellular Ca^{2+} signals, which are responsible for many complex physiological processes ranging from gene transcription and secretion to the more enigmatic brain activities such as learning and memory. Dysfunction of IP_3Rs leads to aberrant Ca^{2+} signaling that is associated with a multitude of human diseases such as Alzheimer's disease, hereditary ataxias, cardiac hypertrophy, heart failure, Parkinson's and Huntington's diseases, atherosclerosis, hypertension and some migraines[1-6].

In mammals, there are three subtypes of IP_3R defined by characteristic features encoded by separate genes, and among them the type 1 IP_3R (IP_3R1) is predominantly expressed in the central nervous system, especially in Purkinje cells of the cerebellum. All IP_3R channels are tetrameric assemblies of monomers of either identical or different subtypes, resulting in channel complexes with a wide range of functional properties. Each IP_3R subunit comprises the pore-forming transmembrane domains (TMDs) and cytoplasmic (CY) domains containing binding sites for ligands and multiple modulators of the channel. These nonselective Ca^{2+} channels are tightly linked to essential phospholipase C-signaling pathways that mediate generation of IP_3 and control a wide range of Ca^{2+}-dependent cellular processes in a highly coordinated manner. Complex cross talk occurring between these pathways and IP_3R channels leads to precise regulation of intracellular Ca^{2+} levels. However, an in-depth understanding of the comprehensive mechanism governing control of intracellular Ca^{2+} dynamics is still lacking.

IP_3Rs work as signaling hubs through where diverse cellular inputs like IP_3, Ca^{2+}, ATP, thiol modifications, phosphorylation and interacting proteins are processed and then integrated to result in cytosolic Ca^{2+} signals with precise temporal and spatial characteristics. IP_3 and Ca^{2+} are the primary agonists of IP_3R channels and both are required for channel opening. Moreover, to fulfill their many physiological roles *in vivo,* IP_3Rs associate with an array of regulatory molecules ranging from ions and small chemical compounds to proteins[7,8]. Unique interactions with these intracellular messengers contribute to the specificity, duration and shape of Ca^{2+} signals generated by IP_3Rs and the channel's capacity to integrate signals from different pathways. A single IP_3 binding site exists at the N-terminus on each IP_3R subunit and functional studies suggest that binding of IP_3 to each monomer is required for channel opening[9]. Important, IP_3 has little effect in the absence of its co-agonist Ca^{2+}. Multiple Ca^{2+} binding sites have also been predicted[7,10]. IP_3R channel opening is modulated with a biphasic dependence on cytosolic Ca^{2+} concentrations, suggesting that the channel has distinct types of Ca^{2+} binding sites for activation and inhibition. Electrophysiological studies showed that the IP_3-evoked activity of IP_3R is enhanced by modest increases in cytosolic Ca^{2+} concentration in the sub-μM range (<1 μM), while higher micromolar concentrations of Ca^{2+} are inhibitory to IP_3 responses[11-13]. ATP is known to enhance the IP_3-induced Ca^{2+} release, by specific binding to IP_3R[12,14-22].

Despite more than three decades since the discovery of IP_3Rs, the detailed molecular and structural mechanisms underlying the complex interplay between ligands, allosteric modulators and channel gating remains unresolved. With the resolution revolution in single particle cryogenic electron microscopy (cryo-EM), there have been remarkable advances in structural characterization of IP_3R [23-28]. These studies reported that the IP_3R structure undergoes conformational changes upon the ligand binding, suggesting structural flexibility of the IP_3R protein that allows the channel to switch from a closed state, capable of interacting with its ligands such as IP_3 and Ca^{2+}, to an open state, capable of transferring Ca^{2+} ions across the ER membrane. However, all of these 3D cryo-EM structures represent defined static conformations of the channel, and the mechanistic insights are derived based on interpolations between discrete structures, each of them likely a combination of dynamic conformational ensemble. Therefore, mechanistically it remains poorly understood how ligands engage the ligand-binding domains and

how multiple signals are coordinated and processed within the IP_3R channel. This implies the necessity to consider the dynamic conformational landscape of the channel protein in determining the molecular mechanisms underlying its function.

In this work, we thought to determine the structures of the IP_3R channel trapped in physiologically relevant states using key ligands that target channel gating. Here, we report cryo-EM structures of IP_3R1 bound to IP_3, ATP and Ca^{2+} and only Ca^{2+}-bound IP_3R1 at overall resolutions of 3.50 Å and 3.26 Å, respectively. In addition, we used a deep neural network approach[29] to extract dynamic features of the IP_3R1 structure directly from 2D cryo-EM images. Our structural findings and hypothesis were validated through mutagenesis and electrophysiology (see also [30]). From these studies, we correlate protein conformational changes that connect the ligand-binding regulatory sites to the channel gate. Our study provides a structural framework for understanding the allosteric mechanisms underlying ligand-mediated IP_3R activation and regulation.

RESULTS

Inherently dynamic architecture of IP_3R1

To elucidate allosteric coupling mechanisms underlying ligand-binding and gating kinetics of the IP_3R channel, we isolated native, Ca^{2+} permeable IP_3R1 channels and used cryo-EM single particle analysis to solve the channel structures in distinct ligand-bound conformations. As the membrane environment is relevant for the functionality of channels, we studied IP_3R1 reconstituted into lipid nanodisc[27]. IP_3 and Ca^{2+} are imperative ligands to trigger the channel opening and ATP increases the open probability of IP_3R1 by synergizing with the activating effect of these two primarily ligands[15,17,18,21,31-34]. The purified IP_3R1 binds IP_3 in a stoichiometric manner (one IP_3 per IP_3R1 monomer) with an affinity of 2-100 nM while functional IP_3 affinities vary from the nanomolar to low micromolar range with mean values for maximum effect around 10 μM, dependent on the technique used[9,35,36]. Ca^{2+} regulates IP_3R1 gating with positive and negative feedback acting in a bell-shaped manner with maximum channel open probability at low μM free Ca^{2+}, while high μM Ca^{2+} inhibits the channel[11,22,37-41].

Hence, the cryo-EM 3D reconstructions of the nanodisc-reconstituted IP_3R1 channels were determined in the presence of saturating IP_3 concentration (10 μM), ~2 μM Ca^{2+} and 1 mM ATP (Ca^{2+}/IP$_3$/ATP-bound IP_3R1; CIA-IP_3R1), and using 20 μM Ca^{2+}, as the sole ligand (Ca^{2+}-bound IP_3R1, Ca-IP_3R1), at estimated overall resolutions 3.50 and 3.26 Å, respectively (Extended Data Figs. 1-4). The final reconstructions are in excellent agreement with the previously solved cryo-EM structures of IP_3R1[23,24,27] and of sufficient quality to allow constructing the atomic structural models for almost the entire protein enabling reliable assignment of most of the side chains (Extended Data Figs. 1-4, 7a, b). Cross-validation between the atomic models and the final density maps suggested that the average resolution of structures was around 3.80 Å and 3.50 Å for CIA-IP_3R1 and Ca-IP_3R1, respectively (Extended Data Figs. 2c, 4c).

The IP_3R structure has a large solenoid CY assembly built around the central helical bundle made of the C-terminal domains from four IP_3R1 subunits (Extended Data Figs. 6a, b). The solenoid scaffold includes domains responsible for binding of ligands and regulatory proteins and is connected via an allosteric nexus at the cytosolic-membrane interface to the TM channel

assembly. Six TM helices from each subunit form the central ion-conduction pore and are well resolved in both the Ca^{2+}- and CIA-bound structures owing to the stabilizing effect of lipid nanodisc (Extended Data Figs. 7a, b).

Local resolution analysis showed that the central TM helices and ligand-binding domains (LBDs) had the highest resolution at 2.4-3 Å, while the cytoplasmic ARM2 domains had the lowest resolution, suggesting that this domain possesses structural flexibility (Extended Data Figs. 2c, 4c). Of note, this domain was poorly resolved in all previous cryo-EM studies of IP_3Rs[23-28]. To improve map quality and local resolution in the ARM2 domain, we performed iterative focused refinements using a mask encompassing the ARM2 domain (Extended Data Figs. 1, 3). The resulting cryo-EM maps are substantially improved, enabling atomic modeling of the ARM2 domain. Two distinct ARM2 conformations reflective of specific ligand-bound states of IP_3R1 were determined (Fig. 1, Extended Data Figs. 1, 3, 5). One conformation, hereinafter called 'extended', was observed in the apo- and Ca-IP_3R1 structures. By contrast, in the CIA-bound IP_3R1, the ARM2 domain is moved ~30 Å towards the ARM1 domain from the same subunit and exhibits a conformation distinct from that observed in the Ca-IP_3R1 or apo-IP_3R1, which we have termed 'retracted'.

To gain insights into the conformational landscape of IP_3R1 underlying its discrete ligand-bound states, we carried out a deep learning based analysis of 2D cryo-EM density data[29]. As expected, the IP_3R1 protein exhibits substantial dynamic motions involving both the cytoplasmic and pore domains (Extended Data Video 1). In particular, our analysis captured that the ARM2 domain undergoes concerted motions in both ligand-bound states of IP_3R1 characterized in the current study, as well as in apo-IP_3R1 structure from our previous study[27]. It is notable that ARM2 exhibits essentially similar motion trajectories in all three states, however the amplitude of its motions is increased in the presence of IP_3. This observation suggests that the reversible IP_3-binding process in the IP_3R tetrameric channel is coupled to conformational motions of the ARM2 domain in some way (Extended Data Video 2). Furthermore, the HD domain exhibits pronounced apical motions, and the LNK and ILD domains that form a nexus at the cytosolic-membrane interface, dilate. Noteworthy, these conformational changes are propagated to the HD- ARM3 interaction interface also undergoing structural rearrangements. In the TMD region the global movements are quite notable exhibiting a rotation of the TM assembly relative to the cytosolic LNK/ILD nexus (Extended Data Video 3).

Based on these results, we envision that the ARM2 domain undergoes structural transitions within the dynamic conformational ensemble and this domain flexibility affects the IP_3-binding pocket properties (discussed below). Overall, the observed conformational motions are in good agreement with our earlier proposed model for long-range allosteric conformational coupling between ligand-binding and activation of the channel gate[23,24].

Conformational dynamics of ARM2 govern IP_3 binding

The IP_3-binding pocket is formed at a cleft between a β-trefoil domain, βTF2 (W226-S436) and a helical armadillo repeat, ARM1 domain (P437-R674) (Fig. 2). The preceding βTF1 domain (M1-

K225) works as an IP_3 binding suppressor[23,42-46]. These three domains (also known as ligand-binding domains, LBDs) form a triangular architecture at the apex of the CY assembly[24].

In the CIA-IP_3R1 structure, we observe a strong density bridging the βTF2 and ARM1 domains at the site where IP_3 is expected to bind (Fig. 2). This density accommodates the IP_3 molecule well. The P1 and P5 phosphate groups of IP_3 are predominantly coordinated by residues from the ARM1 domain and the P4 phosphate group interacts with the βTF2 residues. The CIA structure reveals that P4 forms hydrogen bonds with T267, R269, S274. P5 is also involved in extensive interactions with S274, R269, K508, R511, Y567, K569. In contrast, P1 points outside the IP_3-binding cleft and interacts with only R504 and R568, which is consistent with earlier studies demonstrating that this group is significant for IP_3 binding[47]. The three hydroxyl groups, O2, O3 and O6 can form hydrogen bonds with the ARM1 residues, but have a secondary role in binding of IP_3 [48]. The overall geometry and composition of the IP_3-binding pocket are consistent with observations in crystallographic studies of expressed LBDs and cryo-EM studies of IP_3Rs and have been validated by extensive site-directed mutagenesis[23-25,28,42,43,45,46,49,50].

Superimposition of a single subunit from the apo-, Ca^{2+}- and CIA-bound structures shows that IP_3-binding causes rigid-body movements of all three LBDs resulting in a 4 Å closure of the cleft between the ARM1 and βTF2 domains. Notably, there are little intra-domain rearrangements in both βTF domains upon IP_3- and/or Ca^{2+} binding (1.2 Å Cα RMSD) (Fig. 2b; Extended Data Fig. 8). In contrast, the α-helices in the ARM1 domain undergo substantial shifts in the CIA structure with the entire domain moving towards the IP_3 binding pocket (Fig. 2b, c). In particular, the first α-helix in ARM1 (P437-A457) shifts to 12° from its position in the Ca-IP_3R1 or apo-IP_3R1 structures its C-terminal segment (G458-K462) becomes unraveled. Additionally, the two helices in the ARM1 domain (h3: R504-E512; h7: R568-K576), which residues directly contribute to the coordination of IP_3, move ~20° when engaged with IP_3.

Inspection of the interfaces between the LBDs and the ARM2 domain shows that ARM2 interacts with βTF1 and ARM1 domains from the neighboring subunit in both apo-IP_3R1 and Ca-IP_3R1 structures (Fig. 1c, Extended Data Fig. 6). Specifically, the βTF1-ARM2 interface is stabilized by interactions between A75-D85 and R137-A146 from βTF1 with N1336-S1337 and T1301-H1302 from ARM2 (Fig. 1c). Additionally, an interface between the ARM1 and ARM2 domains is formed at M535-A547 and G463-R471 and S1399-R1408, N1346-Q1352 and N1336-E1339, respectively. The ARM1 residues R545, M535, R471 are in position to form hydrogen bond with residues N1346, R1348, E1399 from the ARM2 domain. We found that these specific intersubunit interfaces are perturbed in the CIA structure, resulting in the formation of a smaller interaction area at a new interface located at residues V1391-S1399 and D1433-M1438 of ARM2 and K136-N145 of βTF1 (Fig. 1d).

The functional implication of these domain-domain interactions is, perhaps, to relieve structural constraints imposed at ARM2/βTF1 and ARM2/ARM1 interfaces that would prevent the LBDs to undergo motions crucial for rendering the IP_3-binding pocket conformations either suitable or unsuitable for capturing IP_3. As a result, the ARM1 α-helices shaping the binding pocket undergo structural changes enabling binding of the IP_3 molecule (Fig. 2). It appears that the ARM2

transition between these two distinct conformations correlates with IP_3-binding to the protein. However, mechanistically it remains unclear how IP_3 engages the LBDs and enters its binding pocket - whether it binds by choosing a particular conformation of its binding pocket or pushes LBD conformation into the IP_3-bound complex.

Structural basis for the IP_3-Ca^{2+} interplay in modulating IP_3R1 activity

The importance of coupling between binding of IP_3 and Ca^{2+} in the regulation of the IP_3R gating activity is evident by multiple prior studies[16,31,32,51-53]. However, a mechanistic description of IP_3-Ca^{2+} interplay in regulation of IP_3R activity is still missing. In this study, to understand the structural basis for the modulation of the channel gating with IP_3 and Ca^{2+}, we determined IP_3R1 structures under activating conditions in the presence of 2 μM Ca^{2+} (CIA-IP_3R1) and in the presence of 20 μM Ca^{2+} that produces channel inhibition (Ca-IP_3R1). The cryo-EM structure of Ca-IP_3R1 reveals strong non-protein densities, establishing the presence of five occupied Ca^{2+}-binding sites in each IP_3R1 subunit (Fig. 3). The side chain densities are well resolved in the detected Ca^{2+}-binding sites permitting assignment of coordinating residues for the bound Ca^{2+} ions. Two Ca^{2+}-binding sites are identified within the ligand-binding domains across the inter- and intra-subunit interfaces between βTF2 and βTF1 domains. The first site, Ca-I_{LBD}, is located at an interface between the βTF2 and βTF1' domains from two neighboring subunits. The Ca^{2+} ion in this site is predominately coordinated by carboxyl groups from D426 and D180 residues in βTF2 and βTF1' domains, respectively. Mutagenesis of D426 in the Ca-I_S site abolished Ca^{2+} binding[54]. The second site, Ca-II_{LBD}, is formed across the interface between the βTF2 and βTF1 in the same subunit. This intra-subunit site is composed of two carboxylate oxygen atoms from E283 and backbone carbonyl oxygen atoms from residues K51, K52, F53 and R54 of βTF1 domain (Fig. 3).

Another strong non-protein density is observed in the putative Ca^{2+} sensor region, which we assigned to a bound Ca^{2+} ion, and this Ca^{2+}-binding site is referred to here as Ca-III_S (Fig. 3). This Ca^{2+} ion is stabilized by carboxylate oxygen atoms from residues E1978 and E2042, Q2045, N1981, and N1971, main chain oxygen from T2654 and a secondary coordination shell may be contributed by H1980 and R1982. Noteworthy, none of the cytosolic Ca^{2+} binding sites described here is similar to that of helix-turn-helix (EF-hand) Ca^{2+}-binding proteins. Moreover, alignment of 3D structures of the Ca-III_S site in IP_3R1, IP_3R3 and RyR channel confirms a structural conservation of this Ca^{2+} binding site across both families of Ca^{2+} release channels as demonstrated in our previous studies[30,55]. In our companion study, mutations of these residues markedly affected single channel activity, such that altering the negative charge on either aspartate residue, shifted the [Ca^{2+}] dependence for activation to the left, consistent with an important role of this site in Ca^{2+} activation of IP_3R1 activity[30]. A conserved E2101 (E4033 in RyR1 and E2005 in IP_3R3) was previously proposed to be responsible for Ca^{2+} sensitivity for activation of IP_3R1 and RyR1 channels[56,57], however, this residue does not directly contribute to coordination of a Ca^{2+} ion in the binding pocket, and appears to exert an effect via allosteric interactions with surrounding residues.

By contrast, in the CIA structure, only two cytosolic Ca^{2+} binding sites, Ca-II_{LBD} and Ca-III_S, were occupied with Ca^{2+} ions. The structures of the two cytosolic sites are nearly identical to those

identified in Ca-IP_3R1 except for subtle rearrangements in the loop regions (Extended Data Figs. 6, 9). Given that Ca^{2+}-occupied Ca-II_{LBD} and Ca-III_S sites are detected at both activating (2 μM) and inhibitory (20 μM) Ca^{2+} concentrations, it would thus appear that Ca^{2+} should bind with higher affinity to these two Ca^{2+}-binding sites compared to the Ca-I_{LBD} site, which is occupied only at an inhibitory Ca^{2+} concentration. Hence, one could speculate that the Ca-I_{LBD} site is a possible candidate for an inhibitory Ca^{2+}-binding site, and two other cytosolic Ca^{2+}-binding sites (Ca-II_{LBD} and Ca-III_S) are activating. Consistent with these data, mutagenesis of amino acid residues in the Ca-III_S site alters channel activity. Specifically, neutralizing the negatively charged side chain on two of the residues individually in Ca-III_S shifted the Ca^{2+} required to activate IP_3R to higher concentrations, indicating that these residues are likely components of the Ca^{2+} activation site in IP_3R1[30]. As it might have been anticipated, binding of IP_3 "tunes" Ca^{2+}-inhibition of the IP_3R channel[16,31,32,51-53].

In both the Ca-IP_3R1 and CIA-IP_3R1 structures, two clear densities, which were interpreted as the bound Ca^{2+} ion, are found in the luminal vestibule leading to the selectivity filter (SF) and the central cavity above the SF. One of these Ca^{2+}-binding sites, named Ca-IV_L, is shaped by the side chains of residues D2551, G2550, R2544, H2541, S2545 contributed across the interface between two neighboring subunits (Fig. 3). The second Ca^{2+}-binding site (Ca-V_L) is located in the central cavity, and Ca^{2+} ion bound at this site is ~2.9 Å away from the amide group in the side chain of N2583 suggesting that the bound Ca^{2+} ion is stabilized in a fully hydrated state. Both identified luminal sites, Ca-IV_L and Ca-V_L, hint at a high affinity binding site as they are occupied at relatively low Ca^{2+} concentration. Moreover, the N2583 residue in rodent IP_3R1 corresponds to N2543 in human, and it has been found that the N2543I mutation is closely associated with Gillespie syndrome[58].

Structural dynamics of the ATP-binding pocket

ATP is known to be a crucial extracellular signaling molecule that increases the open probability of the IP_3R channels[12,15-18,21,22]. Previous sequence analysis identified three glycine-rich regions (GXGXXG) in IP_3R, reminiscent of the Walker-A motif found in many ATP-binding proteins[59,60], and were presumed to account for the ATP-sensitivity of IP_3Rs based on functional studies[12,14-20]. Although binding of ATP to these motifs has been shown with expressed polypeptides, site-directed mutagenesis and single channel measurements revealed that the Walker-A motifs are not required for ATP modulation of IP_3R1[19]. At present, there is a substantial lack of structural knowledge about how ATP regulates the channel gating.

In this quest, using single-particle cryo-EM, we characterize the IP_3R1 channel bound to ATP in the presence of its primary activating ligands (CIA-IP_3R1). The CIA-bound structure reveals a previously unseen ATP-binding site located at the interface between the ILD and LNK domains, where clear density is seen (Fig. 4). The ATP molecule fits well into the observed elongated density. Of note, both the apo- and Ca^{2+}-bound structures lack this density. The resolution in the ATP-binding site was of sufficient quality to unambiguously identify the precise pose of the ATP molecule as well as coordinating residues in the binding pocket. Notably, this pose allows formation of hydrogen bonds between the negatively-charged ATP triphosphate tail and residues K2221, K2224, K2633, N2637, W2639. The residues N2637, M2638, W2639, I2632, C2611,

F2612 are responsible for the coordination of the adenine moiety of ATP whereas the residues Y2228, I2632, K2633, N2637, M2638 are involved in the recognition of the hydroxyl groups in the ribose ring of ATP. Therefore, positively charged and hydrophobic residues from ILD and LNK domains coordinate bound ATP molecule within its binding pocket. The architecture of the ATP-binding pocket is structurally conserved across the intracellular Ca^{2+} release channel family, which includes the ryanodine receptors (RyRs) (Fig. 4c, Extended Data Fig.9e).

Detailed comparisons of the ATP-binding pocket in the apo- or Ca^{2+}-bound structures with the CIA-structure reveal that binding ATP causes the most notable change in the side chain conformation of W2639. In the Ca-IP_3R1 and apo-IP_3R1 structures, we found two clear densities where alternative W2639 rotamers can be fitted (Fig 4d, Extended Data Fig.8f). In contrast, only one W2639 side chain conformation was detected in the CIA structure, likely owing to the compatibility of the binding pocket to the ATP molecule. Based on these observations, it appears that ATP binding requires flipping of the W2639 side chain inward towards the binding site working as a 'structural switch' for specific ATP binding to the protein.

Ion conduction pathway

IP_3R channels contain a single ion-conducting pore formed at the interface between the TMDs of four subunits along the four-fold axis of the channel. The central pore is lined by the transmembrane helices TM5 and TM6(Extended Data Fig. 7a). A section of the pore towards the luminal side of the ER membrane, known as the selectivity filter (SF) is shaped by the four luminal P-loops connecting the intervening luminal pore (P) and TM6 helices. The IP_3R1 structures described here have a wide luminal vestibule leading to the SF formed by the conserved residues G2546-V2552 from the P-loop at the luminal side of the ion conduction pathway. The diameter of the SF at the entrance to the central hydrophilic cavity of the pore is narrowest in Ca^{2+}-bound structure (7.5 Å) and widened to ~9.4 Å and 10.7 Å in apo- and CIA-structures, respectively (Fig. 5). Immediately above the SF there is a water filled cavity, where hydrated Ca^{2+} ions can reside.

Both the Ca- and CIA-structures exhibit two physical sites of constriction in the ion channel pore at the conserved F2586 and I2590 residues of the pore-lining TM6 helix, consistent with previous studies[23,24,27]. The F2586 and I2590 side chains form two hydrophobic seals in the middle of the TM6 helix and near the cytosolic side of the pore, respectively (Fig. 5). Superimposition of IP_3R1 structures in apo- versus Ca^{2+}-bound and CIA-bound states shows that IP_3 binding is associated with coordinated structural changes within the ion conduction pathway. In the Ca^{2+}-bound structure, the cross-sectional area at the pore constrictions has the diameter of 6 Å and 5 Å, respectively, as estimated by the distance between side chains from two opposite subunits at F2586 and I2590. These pore dimensions are similar to that in the nanodisc reconstituted apo-IP_3R1 structure, in which the pore is closed, representing non-conducting channel state[27]. In contrast, in the CIA-IP_3R1, the diameter of the ion pathway at F2586 constriction is ~11 Å (Fig. 5). This pore expansion is achieved by 50° rotation of the F2586 side chain away from the four-fold axis and down toward the ER lumen. This side chain rearrangement makes the constricted pore permeable to hydrated Ca^{2+} ions, with a diameter of 8-10 Å [61,62]. However, the pore diameter at the position of I2590 remains ~5 Å as seen in the

Ca-IP_3R1 and apo-IP_3R1 structures (Fig. 5). The ion pathway is too narrow at this location for passage of hydrated Ca^{2+}, but it is wide enough for dehydrated or partially hydrated Ca^{2+} ions. Furthermore, the pore-lining TM6 helix in the CIA- and Ca^{2+}-bound structures of IP_3R1 adopts the π-helix conformation at residues M2576-V2581 residue and confers flexibility to the ion conduction helix bundle (Extended Data Fig. 7c). By contrast, the apo-structure of ND-reconstituted IP_3R1 exhibits straight TM6 helices at this region[27]. On the basis of these observations, we propose that gating in IP_3R1 involves an α -to-π secondary structure transition.

In both the Ca-IP_3R1 and CIA-IP_3R1 structures, the SF and a central cavity are continuous with the luminal solvent, and hydrated Ca^{2+} ions can diffuse into and out of the water filled luminal vestibule of the ion conduction pathway (Fig. 5c, d). Thus, the Ca-V_L site is easily accessible for binding of Ca^{2+}. However, it seems that the occupancy of this Ca^{2+} - binding site is dependent on conformation of the TM6 helix. The TM6 rearrangement upon the channel activation is accompanied by movement of the F2586 side chain in the hydrophobic constriction and shift of the N2583 side chain, which coordinates Ca^{2+} ion in the Ca-V_L site (Fig. 3, Extended Data Fig. 9). This can potentially weaken Ca^{2+}-coordinating interactions or even force loss of Ca^{2+} into the water filled central cavity from where it can travel down the electrochemical gradient *in vivo*.

Overall, the conformation of the ion conduction pore in the CIA-IP_3R1 structure is compatible with that in the IP_3R1 channel characterized in the presence of adenophostin A and Ca^{2+} [24]. We note, however, an additional strong density at the location of F2586 in the pore-lining TM6 helix, where the F2586 side chain can be alternatively docked in the CIA structure. This density points to the central 4-fold axis of the pore and is consistent with the conformation of the F2586 side chain observed in the apo- or Ca-IP_3R1 structures representing the IP_3R channel in closed (non-conducting) state (Fig. 5b). In addition, the structural rearrangements of the SF observed in CIA-structure stand in contrast to what is seen in the IP_3R1 visualized in the presence of activating concentrations of adenophostin A and Ca^{2+} (AdA-IP_3R1), which SF is narrower (~8.5 Å) than that in apo-IP_3R1[24]. These structural differences might reflect the separate contexts in which these structures were determined, CIA-bound in a nanodisc and the other in the detergent[24]. Noteworthy, the narrow dimeter of the SF in apo-IP_3R1 likely does not reflect any physiological state as it is very unlikely that IP_3R channel exists in Ca^{2+}- free state *in vivo*.

To further investigate functionality of the amino acids at the constriction site, mutants of residues F2586 (F2586K) and I2590 (I2590N and I2550T) were generated in human IP_3R1 (hR1). The F2586K mutation replaces a large, hydrophobic Phe with a positively charged Lys, while the I2590N and I2550T mutations are associated with human disease[58,63,64] The mutations were stably overexpressed in cells engineered via CRISPR/Cas9 to lack all three endogenous IP_3Rs (HEK-3KO)[9] (Fig. 6a, b), All three mutations resulted in significantly decreased amplitude of agonist-induced Ca^{2+} release (Figure 6c, e) when compared with the null cell line, an endogenously expressed human IP_3R1 control (Endo. hR1), and an exogenously expressed human IP_3R1 control (Exo. hR1). The basal [Ca^{2+}] was not altered in any of the mutations (Fig. 6c, d). Replacing F2586 with the positively charged K creates electrostatically unfavorable environment for the permeating Ca^{2+} via the open pore (Ca^{2+} blockage). The presence of neutral T or hydrophilic N at the I2590 position is clearly not favorable for inter-subunit hydrophobic side-

chain packing that will perturb the pore stability thereby affecting the channel open probability. Thus, our results confirm the critical nature of the F2586 and I2590 residues in IP_3R1 channel function.

DISCUSSION

The high-resolution structures of Ca^{2+}- and Ca^{2+}/IP_3/ATP-bound IP_3R1 presented in this study highlight the correlation between the protein dynamics and its propensity for accepting multiple cellular signals that regulate the channel activities, such as ligand-binding, gating and regulation. Considering the remote distances between the cytoplasmic ligand-binding sites and ion conduction pathway in the channel, the intrinsically flexible 3D architecture of the IP_3R provides the basic premise behind the allosteric regulation of the channel activity that involves the transfer of ligand-evoked signals from the distinct ligand-binding domains to the ion conducting channel gate (Fig. 7). This process is mediated through molecular interactions at inter- and intra-domain interfaces embedded in the conformational landscape of the protein. While some structural features of the ligand-bound IP_3R1 that we highlighted here confirm our previous observations[23,24], the present study reveals mechanisms for the conformational transitions underlying IP_3R1 activity.

In particular, using a deep-learning technique, we observe that the ARM2 domain exhibits the unique motions within the dynamic conformational ensemble, resulting in two predominant conformations seen in CIA- and Ca^{2+}- bound states. In the IP_3-binding process in the context of the tetrameric channel assembly, intrinsic flexibility of the ARM2 domain is highly important as its dynamic behavior perhaps allows to release structural constraints imposed at interaction interfaces between LBD and ARM2 domains that facilitates the conformational selection from a pre-existing ensemble of IP_3-binding pocket conformations and promotes specific binding of the IP_3 molecule. Based on our results, the dynamic interactions between the ARM2 and LBD domains can be envisioned as ‘a reversible ratchet' mechanism with the gear (ARM2) held in place by its contacts with βTF1 and ARM1 domains from the neighboring subunit (Fig. 7a). This dynamic re-arrangement allows direct (clockwise) as well as reverse (counterclockwise) movements of the ARM2 between ‘extended’ and ‘retracted’ positions with the latter favorable for specific binding of IP_3. Altogether, these results allow us to delineate distinct steps in IP_3-binding conformational cycling, including interfacial rearrangements. It appears that IP_3 may work by tuning the Ca^{2+} sensitivity of IP_3R1 by decreasing the Ca^{2+} affinity of the Ca-I_{LBD} site and stimulating Ca^{2+} binding to the Ca-II_{LBD} site. The conformational changes observed in the IP_3-binding domains unequivocally propagate through other cytoplasmic domains to the TMDs that form the channel pore (Fig. 7).

It is important to note that our high-resolution CIA-IP_3R1 structure demonstrates that under saturating activating conditions used in this study, the gating state of the channel pore likely relies on conformational dynamics of the F2586 side chains that can potentially alter the relative stability of conformational states of the pore. Hence, instead of directly going from closed to open conformation, the pore-forming elements can adopt a mixture of conformations resulting in different levels of IP_3R1 channel activity observed under constant experimental conditions in electrophysiological studies[65,66]. This phenomenon known as modal gating has been observed in many other ion channels including RyR Ca^{2+} release channel[67-72].

While the observed degree of the pore opening at I2590 in the CIA structure is not as wide as a hydrated Ca^{2+} ion, it might provide a Ca^{2+} ion passage using a different mechanism relying on dynamic side chains shaping this hydrophobic constriction. Noteworthy, it has been demonstrated that the pore in structures of several K^+ channels and the human CLC-1 chloride channel are not wider than a hydrated ion under activating conditions[73-78]. Thus, a slightly narrow tunnel lined with dynamic side chains apparently can provide a good passage for ions.

The presence of the π-gating hinge in IP_3R1 channel is consisted with structures of IP_3R3 channel, solved by cryo-EM[25,28], suggesting that gating in both channel types are prone to α-to-π transitions. However, the detergent-solubilized IP_3R3 channel exhibits the π-helix in TM6 in the non-conducting (closed) state, which transitions to an α-helix in the presence of IP_3 and Ca^{2+}. Strikingly, unlike IP_3R3, the ligand-bound structures of IP_3R1 reconstituted into lipid nanodisc solved in this study, appear to favor the π-helix upon the channel activation. Together, these data suggest that the lipid environment plays an essential role in formation and maintenance of π-helix structure.

Furthermore, the results of the present study are supportive of the importance of side chain dynamics in ATP binding by IP_3R1 protein. Studies suggest that the three IP_3R isoforms exhibit different sensitivity to ATP with IP_3R1 being enhanced by micromolar ATP and IP_3R3 being augmented by millimolar ATP, whereas IP_3R2 is more sensitive to ATP but only at sub-micromolar IP_3[14,79,80]. Our analysis revealed a side chain conformational preference for W2639 that contributes to ATP binding. This observation supports the hypothesis that ATP-binding specificity of IP_3Rs might be mediated by the recognition of specific rotameric states of key residues in the ATP-binding pocket. Additionally, the presence of conserved lysine residues responsible for the coordination of ATP phosphates in IP_3R1 likely contribute to isoform specific ATP binding affinity. Decoding the structural basis of exquisite isoform specificity with respect to a modulatory role of ATP in the IP_3R family will certainly be critical in future studies.

Overall, our analysis exposes a structural mechanism for the susceptibility of IP_3R1 to binding of IP_3, based on the conformational selection of the ligand-binding pocket, which may adapt different conformations in its unbound state for which IP_3 binds selectively to one of these conformations. We propose that IP_3/Ca^{2+}-evoked gating involves 'a conformational wave' that unequivocally propagates via the cytoplasmic domains towards the pore-forming TMDs (Fig. 7, Extended Data Videos 1-3). The present results highlight a key role of specific interactions in the side chain network surrounding the ion conduction path in regulating gating behavior of IP_3R channels. Notably, the structural rearrangements in the cytoplasmic domains are substantial relative to the transmembrane domain suggesting that the structural flexibility allows the protein domains to adapt to their individual molecular binding partners facilitating the binding process. Our study provides a firm structural framework for interpreting large amounts of functional and biochemical data accumulated during more than three decades of research targeting IP_3-mediated Ca^{2+} release. However, further systematic work combining structural analysis with site-directed mutagenesis and electrophysiological characterization is still needed to test connections between

functional paths and protein motions underlying ligand-mediated allosteric information transfer within the channel.

METHODS

IP_3R1 purification and reconstitution into nanodiscs

Purification of neuronal IP_3R1 reconstituted was performed as previously described[27,44]. Briefly, rat cerebellar membranes were solubilized in 2 mM Lauryl Maltose Neopentyl Glycol (LMNG, Anatrace) and 0.1% (w/v) l-α-phosphatidylcholine (PC, Sigma) for 2 h at 4 °C. Non-solubilized material were cleared by ultracentrifugation (100,000 x g) and the supernatant was applied to an immunoaffinity matrix pre-coupled with monoclonal antibodies (T433 epitope of IP_3R1) in 50 mM Tris-HCl (pH 7.4), 150 mM NaCl, 1 mM DTT, 1 mM EDTA, 0.02 mM LMNG. Reconstitution of IP_3Rs into lipid-nanodiscs occurred "on-column" as we described in [27]: 1.2 mM POPC (1-palmitoyl-2-oleoyl-glycero-3-phosphocholine, Avanti Polar Lipids) prepared in 3% DDM (n-dodecyl-β-d-maltoside, Avanti Polar Lipids, Inc), 50 mM Tris-HCl (pH 7.4), 150 mM NaCl, 1 mM DTT, 1 mM EDTA was added to the IP_3R1-bound immunoaffinity column matrix followed by the addition of 0.6 mg/ml MSP1E3D1 (Cube Biotech). Detergent removal was achieved by the addition of 0.25 mg/ml activated Bio-Beads-SM2 (BioRad) for 16 h at 4 °C. IP_3R1 was eluted with 500 µM of T433 peptide and concentrated using a 100 kDa Amicon centricon (Millipore).

CryoEM sample preparation and data acquisition

The nanodisc reconstituted purified IP_3R1 (2 mg/ml) was vitrified after 30 min in incubation with 20 µM free Ca^{2+} to obtain the structure of IP_3R1 bound with Ca^{2+} (Ca-IP_3R1) or with 2 µM free Ca^{2+}, 10uM of IP_3 and 1mM ATP to obtain Ca/IP3/ATP-bound IP_3R1 (CIA-IP_3R1). Vitrification of the IP_3R1 samples was performed using a Vitrobot Mark IV (ThermoFisher Scientific, Inc.) as described earlier [27]. Blotting was done with filter paper filter paper Whatman 542 containing 8-14 µg Ca/g paper (Whatman). The final free Ca^{2+} concentrations were determined using MaxChelator (http:// maxchelator.stanford.edu/oprog.htm). CryoEM data acquisition was performed with a Titan Krios microscope (ThermoFisher Scientific, Inc.) operated at 300keV, equipped with a BioQuantum energy filter (Gatan, Inc.) with zero-loss energy selection slit set to 20 eV. All data sets were acquired using the EPU software (ThermoFisher Scientific, Inc.) at a nominal TEM magnification of 130,000× and recorded on a K2 Summit direct electron detector (Gatan, Inc.) operated in super-resolution counting mode with a calibrated physical pixel size of 1.07 Å. The data acquisition parameters (total movie stacks, dose rete, total dose, defocus range, etc.) are summarized in Table 1.

Image processing

Movie stacks were motion corrected with dose weighting and binned 2 × 2 by Fourier cropping resulting in a pixel size of 1.07 Å using MotionCor2[81]. The motion-corrected micrographs were evaluated by 'e2evalimage.py' in EMAN2[82] and were used for all the following image processing. Contrast transfer function (CTF) determination was performed using Gctf[83]. Particles were picked using the NeuralNet autopicking procedure implemented in EMAN2 and the .box files were imported to RELION3[84] and were subjected to iterative 2D and 3D classification. Our previously resolved cryo-EM map of apo-IP_3R1 (Electron Microscopy Data

Bank (EMDB): EMD-23337) was low-pass filtered to 60 Å as a starting reference map. After 3D auto-refinement, two overall 3D reconstructions at 3.50 Å and 3.26 Å resolution (using FSC at 0.143[85]) were generated for the CIA-IP_3R1 and Ca-IP_3R1 respectively (Extended Data Fig. 2, 4). Local resolution estimation was performed by Resmap[86], the results show ARM2 domain is the most flexible region of the IP_3R1 map. To improve the map quality of ARM2 domain, we performed symmetry expansion by running the command "relion_particle_symmetry_expand" with C4 symmetry, followed by multiple rounds of 3D classification, and the strongest classes were subjected to local refinement with a mask including only ARM2 domain (Extended Data Figs. 1-5). The expanded concensus particles were imported to cryoSPARC[87] or EMAN2, and were used to analyze the conformational dynamics of the particles by the 3D Variability Analysis in cryoSPARC[88] or GMM in EMAN2[29] . Flow charts for data processing steps are presented in Extended Data Figs 1, 3, 5.

Model building

We utilized a consistent approach for protein model building in both CIA-IP_3R1 and Ca-IP_3R1 cryo-EM density maps. Our previously published cryo-EM structure of apo-IP_3R1 in nanodisc (PDB ID: 7LHE) was used for rigid body fitting in UCSF Chimera[89] followed by an initial round of flexible fitting of the IP_3R1 subunit in COOT. Density modification "phenix.resolve_cryo_em" was performed on the half-maps resulting in improved resolvability in the density maps allowing for further model optimization. AlphaFold[90] was used to generate optimized models for each of the 10 domains within an IP_3R1 subunit using the initial IP_3R1 model for each domain as a template. The results were then concatenated and tetramerized in Chimera, refined against the density map with "phenix.real_space_refine" with default options and manual optimization in Coot to maximize fit to density, minimize Ramachandran angle outliers and eliminate steric clashes. The ligands were fit to the masked densities and refined along with the protein model using "phenix.real_space_refine". Model validation was carried out using EMRinger and MolProbity in PHENIX. Map-model visualization was performed in Coot and UCSF Chimera. Interfaces described in the paper were identified with PDBePisa[91], ChimeraX[92] LigPlot+[93] and HOLE [94]. Figures and movie were prepared using UCSF Chimera; ChimeraX and VMD 1.9.4[95].

Generation of IP_3R Mutants

A two-step QuikChange mutagenesis protocol was used to introduce amino acid substitutions into cDNA encoding the human IP_3R1 (hIP_3R1; NM_001099952in pDNA3.1 (Obtained from Annetta Wronska at Columbia University). Mutagenesis and all DNA modifications were carried out using *Pfu* Ultra II Hotstart 2X Master Mix (Agilent). Mutagenesis primers for hIP_3R1 F2586K forward (TCTTCATGGTCATCATCATTGTTCTTAACCTGATTAAGGGGGTTATCATTGACACT), hIP_3R1 F2586K reverse (AGTGTCAATGATAACCCCCTTAATCAGGTTAAGAACAATGATGATGACCATGAAGA), hIP_3R1 I2590N forward (TTGGGGTTATCAATGACACTTTTGCTGACCTACGTAGTGAGAAGCAG), hIP_3R1 I2590N reverse (CTGCTTCTCACTACGTAGGTCAGCAAAAGTGTCATTGATAACCCCAA), hIP_3R1 I2590T forward (TTGGGGTTATCACTGACACTTTTGCTGACCTACGTAGTGAGAAGCAG), and hIP_3R1 I2590T reverse (CTGCTTCTCACTACGTAGGTCAGCAAAAGTGTCAGTGATAACCCCAA), were synthesized by Integrated DNA Technologies (IDT). In addition to encoding the specified mutations, primers

also silently introduced a restriction site for verification purposes. The coding regions for all constructs were confirmed by sequencing.

Cell Culture and Generation of HEK cell lines stably expressing IP_3R Monomers

HEK-3KO cells, HEK293 cells engineered through CRISPR/Cas9 for the deletion of the three endogenous IP_3R isoforms[96] and HEK293 cells modified by CRISPR/Cas9 to only express endogenous hIP_3R1 (Endo. hR1) were grown at 37˚C with 5% CO_2 in Dulbecco's Modified Eagle Medium (DMEM) supplemented with 10% fetal bovine serum, 100 U/ml penicillin, 100 µg/ml streptomycin (Gibco/Life Technologies). Transfection of HEK-3KO cells to exogenously express desired hIP_3R1 WT or mutant constructs stably was performed as previously described [96]. In brief, 5 million cells were pelleted, washed once with PBS, and resuspended in either Nucleofector Solution T (Lonza Laboratories) or a homemade transfection reagent (362.88 mM ATP-disodium salt, 590.26 mM $MgCl_2$ 6.H_2O, 146.97 mM KH_2PO_4, 23.81mM $NaHCO_3$, and 3.7 mM glucose at pH 7.4). 4-6 µg of DNA was mixed with the resuspended cells and electroporated using the Amaxa cell nucleofector (Lonza Laboratories) program Q-001. Cells were allowed to recover for 48 hours before passage into new 10 cm plates containing DMEM media supplemented with 2 mg/ml Geneticin sulfate (G418; VWR). Following 7 days of selection, cell colonies were either picked and transferred to new 24-well plates or diluted into 96 well-plates, both of which contained DMEM media supplemented with 2 mg/ml G418. Diluted wells in the 96-well plate were screened after 7 days for the presence of a single colony of cells growing in each well. Those wells that exhibited multiple colonies growing were excluded from further consideration. 10-14 days after transfection wells – both 96 and 24 - that exhibited growth were expanded and those expressing the desired constructs were confirmed by western blotting.

Cell Lysis and SDS-PAGE Analyses

DT40-3KO cells, HEK-3KO cells, or DT40-3KO and HEK-3KO cells stably expressing IP_3R constructs were harvested by centrifugation (200 x *g* for 5 min), washed once with PBS, and solubilized in membrane-bound extraction lysis buffer containing 10 mM Tris-HCl, 10 mM NaCl, 1 mM EGTA, 1 mM EDTA, 1 mM NaF, 20 mM $Na_4P_2O_7$, 2 mM Na_3VO_4, 1% Triton X-100 (v/v), 0.5% sodium deoxycholate (w/v), and 10% glycerol supplemented with a cocktail of protease inhibitors (Roche, USA). Lysates were incubated for a minimum 30 min on ice and cleared by centrifugation (16000 x *g* for 10 min) at 4°C. Protein concentrations in cleared lysates were determined using D_c protein assay kit (Bio-Rad) and 4x SDS gel loading buffer was subsequently added to 5 µg of lysate. Proteins were resolved using 8% SDS-PAGE and subsequently transferred to a nitrocellulose membrane (Pall Corporation). Membranes were probed with a rabbit polyclonal antibody against the C-terminal 19aa of IP_3R1 (CT1; #ARC154, Antibody Research Corporation) at a 1:1000 dilution, GAPDH (#ARC154, Antibody Research Corporation) at a 1:75,000 dilution, and the appropriate Dylight™ 800CW secondary antibodies at a 1:10,000 dilution (SA535571 and SA535521; Invitrogen). Membranes were imaged with an Odyssey infrared imaging system and quantified using Image Studio Lite (LICOR Biosciences).

Single Cells Ca^{2+} Imaging: Measurement of Cytosolic Ca^{2+} in Intact Cells

Single cell Ca^{2+} imaging was performed in intact cells as described previously[96]. Glass coverslips were plated with HEK-3KO, Endo. hR1, Exo. hR1, or HEK-3KO cells stably expressing IP_3R mutant constructs at least 18 hours prior to imaging experiments. Subsequently, the glass coverslips were mounted onto a Warner chamber and the cells were loaded with 2 µM Fura-2/AM (Molecular Probes) in Ca^{2+} Imaging Buffer (Ca^{2+} IB;10 mM HEPES, 1.26 mM Ca^{2+}, 137 mM NaCl, 4.7 mM KCl, 5.5 mM glucose, 1 mM Na_2HPO_4, 0.56 mM $MgCl_2$, at pH 7.4) at room temperature for 25 minutes. Following loading, cells were then perfused with Ca^{2+} IB which provided a basal 340/380 ratio of the [Ca^{2+}] and stimulated with 3 µM. 30 µM, and 100 µM carbachol (CCh) to obtain measurements of agonist-induced Ca^{2+} release into the cytoplasm.

Ca^{2+} imaging was performed using an inverted epifluorescence Nikon microscope with a 40x oil immersion objective. Cells were alternately excited at 340 and 380 nm, and emission was monitored at 505 nm. Images were captured every second with an exposure of 15 ms and 4 × 4 binning using a digital camera driven by TILL Photonics software. Image acquisition was performed using TILLvisION software and data was exported to Microsoft Excel where the means were calculated. Statistical analysis of at least n=3 experiments for each cell line was performed in GraphPad Prism (one-way ANOVA with Tukey's test).

Data availability

Coordinates and corresponding EM maps of the CIA-IP_3R1 (PDB: xxxx; EMDB: EMD-xxx) and Ca-IP_3R1 (PDB: xxxx; EMDB: EMD-xxx) have been deposited in the Protein Data Bank (http://www.rcsb.org) and the Electron Microscopy Data Bank (https://www.ebi.ac.uk/pdbe/emdb/), respectively.

Acknowledgements

We thank Venkata Mallampalli at CryoEM Core Facility at UTHealth at Houston for technical support on cryo-EM. This work was supported by grants from the National Institutes of Health (R01GM072804 to I.I.S; DE019245 to D.I.Y; R01GM080139 to S.J.L.), American Heart Association grant (18CDA34110086 to M.R.B) and Welch Foundation research grants (AU-2014-20190330 & AU-2014-20220331 to I.I.S). TFS Titan Krios Equipment subsidized by CPRIT Core Facility Award RP190602 was used for Cryo-EM imaging in this work.

Author Information

Muyuan Chen's present address: SLAC National Accelerator Laboratory, 2575 Sand Hill Rd; Mailstop 0027; Menlo Park, CA 94025, USA

Contributions: I.I.S. and D.I.Y. conceived the project; G.F, M.R.B., A.B.S prepared samples of IP_3R1; GF collected cryo-EM data and determined structures; G.F., M.R.B. and M.L.B. built and refined the atomic models; G.F, M.R.B., M.L.B and I.I.S. analyzed the structures; S.J.L., M.C. and G.F performed variability analysis; L.E.T and V.A made mutations in IP_3R and performed functional analyses of IP_3R activity; I.I.S. wrote the paper with the help from M.R.B. and G.F., and all other co-authors.

These authors contributed equally: Guizhen Fan and Mariah R. Baker

Corresponding authors: David I. Yule (David_Yule@URMC.Rochester.edu) and Irina I. Serysheva (irina.i.serysheva@uth.tmc.edu).

Ethics declarations

Competing interests:The authors declare no competing interests.

FIGURE LEGENDS

Figure 1. Distinct domain conformations of ligand-bound IP_3R1 structures. Cryo-EM density maps and corresponding models of Ca^{2+} bound IP_3R1 **(a)** and Ca^{2+}/IP_3/ATP bound IP_3R1 (**b**) viewed along its four-fold axis from the cytosol. Domains involved in distinct conformational changes (in two subunits) are labeled. Bound IP_3 density is colored magenta. The neighboring subunit is indicated by a single quote symbol. Molecular models for ligand-binding and interfacial domains are rendered as pipes and planks for Ca-IP_3R1 (**c**) and CIA-IP_3R1 (**d**). ARM2 inter-subunit interfaces are indicated by boxes and enlarged in the lower panels. Zoomed in boxed areas depict the amino acids present at the molecular interfaces. The red asterisk identifies the same helix in each structure. **f,** HD and ARM2 domains from an aligned subunit from Ca-IP_3R1 (tan) and CIA-IP_3R1 (colored by domain) are superimposed. Arrows indicate 32 Å rotation of ARM2 and a 10 Å translation of HD.

Figure 2. IP_3 induced conformational changes in the ligand binding pocket. a, The IP_3 molecule is fit to the density bridging βTF2 and ARM1 domains in the CIA-IP_3R1 cryo-EM map overlaid with the corresponding molecular model (left panel). Zoomed-in view of the IP_3 binding pocket structure with coordinating side-chain residues indicated (right panel). **b,** Alignment of CIA-IP_3R1 and Ca-IP_3R1 models at the βTF1 domain shows the closure of the IP_3 binding pocket and nearly identical βTF1 and βTF2 backbone structures. **c,** ARM2 helices in CIA-IP_3R1 are shifted toward the occupied ligand binding pocket. ARM2 domains (CIA-IP_3R1 colored green; Ca-IP_3R1 colored tan) are shown as thin ribbons overlaid with helices rendered as cylinders and numbered sequentially within the domain. The IP_3 molecule is white.

Figure 3. Ca^{2+} binding sites in Ca-IP_3R1. a, Ca^{2+} binding sites localized in the ligand binding domain (Ca-I_{LBD} and Ca-II_{LBD}), Ca^{2+} sensor in ARM3 domain (Ca-III_s), and luminal vestibule of the TMD (Ca-IV_L and Ca-V_L) from the Ca-IP_3R1 structure are shown for a single subunit (white) with the region surrounding the Ca^{2+} binding site highlighted in color. Lower panel shows a view from the lumen along ion conduction pathway in the tetrameric Ca-IP_3R1 structure. **b,** Zoomed-in views of the Ca^{2+} binding sites. Ca^{2+} ions are shown as green spheres and overlaid with corresponding densities displayed at 2-5 σ cutoff values. Residues within 5 Å of the Ca^{2+} ions are displayed in a stick representation and labeled.

Figure 4. Structural determinants and dynamics in the ATP binding pocket. a, Localization of the ATP binding site in the CIA-IP_3R1 structure colored by domain and overlaid with cryo-EM densities in gray. The ATP molecule fits to the additional density (indicated by the mesh density) observed between the ILD and LNK domains, colored blue-green and orange respectively. **b,** Zoomed-in view of the ATP binding pocket with the ATP densities shown in gray mesh; side-chain residues within 5 Å of the ATP molecule are displayed. A zinc ion (overlayed with densities at ~15σ) is located within the C2H2-like Zn^{2+} finger domain adjacent to the ATP binding pocket. **c,** Conserved 3D architecture of the ATP binding pocket for CIA-IP_3R1 (blue-green) and RYR (gold) shown as thin ribbon models and ATP molecule shown in sticks. ATP within the RyR1 binding pocket is angled 40° toward the membrane plane with respect to the bound ATP in CIA-IP_3R1. Zoomed-in view of cryoEM density maps for CIA-IP_3R1 (**d**) and Ca-IP_3R1 (**e**) overlaid with their respective molecular models focused on the side chain conformers

for W2639. ATP molecule is fit to the mesh density in 'd'. **f,** Schematic plot of the ATP molecule interacting with surrounding side chains in CIA-IP_3R1 structure. Arcs represent hydrophobic interactions, green dashed lines are H-bonds as calculated in LigPlot+[93].

Figure 5. Ion conduction pathway in IP_3R1 upon ligand binding. a, The ion conduction pathway in CIA-IP_3R1 (blue-green), Ca-IP_3R1 (pink), apo-IP_3R1 (PDB ID: 7LHE, tan) are aligned and overlaid. Show for clarity are the backbone structures for two opposing subunits with several solvent lining side chains shown and labeled. Red arrow indicates the change in side chain position of F2586 observed in CIA-IP_3R1. Upper right panels show zoomed in views of the area indicated by the box in the left panel. Distances across the ion conduction pathway at I2590 and F2586 are measured from side-chain atoms from two opposite subunits. **b,** Cryo-EM densities overlaid with atomic models for the TM6 gate residue F2586. Two rotomers of F2586 (orange and blue-green) are shown for CIA-IP_3R1. Densities in Ca-IP_3R1 and apo-IP_3R1 permit only one rotamer fit for F2586. **c,** Solvent-accessible pathway in CIA-IP_3R1, Ca-IP_3R1 and apo-IP_3R1. The left panel plots the pore dimensions along the ion conduction pathway and the right panels reveal the solvent accessible volume. **d,** Luminal view of the selectivity filter (2544-RSGGGVGD-2551) for CIA-IP_3R1, Ca-IP_3R1, and apo-IP_3R1 at the region indicated by black arrows in 'a' and colored respectively. Distance across the SF is measured between the G2546 $C\alpha$ atoms from two opposite subunits.

Figure 6. Functional validation of gating residues in ion conduction pathway. a, Immunoblots of lysates prepared from the indicated HEK cell lines. HEK-3KO and endogenous hIP_3R1 (Endo. hIP_3R1) were generated by CRISPR/Cas 9 technology, the former is null for all IP_3R subtypes while the latter expresses only IP_3R1. Mutations and exogenously expressed IP_3R1 (Exo. hR1) were stably expressed in HEK-3KO cells. All stable clonal cell lines result in expression levels above that of Endo. hIP_3R1, as quantified in 'b'. **c**, Representative single cell Ca^{2+} traces in fura-2 loaded HEK cell lines stimulated with increasing concentrations of the muscarinic agonist carbachol (CCh). **d**, Basal fluorescence, prior to stimulation in HEK cell lines. **e**, Pooled data depicting the response of cell lines to CCh stimulation. *significantly different from Endo. hIP_3R1. #significantly different from Exo. hIP_3R1. ###/***$p< 0.001$; ##$p<0.01$, #$p< 0.05$ ANOVA.

Figure 7. Schematics of ligand-induced structural changes underlying activation of IP_3R1 channel. a, A conformational wave generated upon binding of the activating ligands propagates from the LBDs forming the apical portion of the channel via the LBD/LNK assembly ('nexus') towards the channel pore. Depicted are two opposing subunits colored by domains. Domain motions are indicated with arrows. **b**, Conformational changes underlying binding of IP_3, Ca^{2+} and ATP. Intrinsic flexibility of ARM2 domain allows for a reversible ratcheting mechanism where ARM2 switches between 'extended' and 'retracted' conformations. The extended conformation is restrictive for binding of IP_3 (top left), while 'extended' conformation is suitable for capturing IP_3 due to release of structural constraints at interfaces between ARM2 and βTF1' and ARM1' from the neighboring subunit (top right). Allosteric nexus comprising LNK and ILD domains (middle panels) and the channel pore at F2586 (bottom panels) are expanded in the

presence of activating ligands. The domains in Ca-IP_3R1 (left column) and CIA-IP_3R1 (right column) structures are viewed along the central 4-fold axis from the cytosol with one subunit outlined in black.

Extended Data Figure Legends

Extended Data Figure 1. Cryo-EM processing workflow for Ca-IP_3R1.

Extended Data Figure 2. Characteristics of cryo-EM reconstructions for Ca-IP_3R1. a, Euler angle distribution of particles contributing to the final reconstruction with larger red cylinders representing orientations comprising more particles. **b**, Resolution estimation of the cryo-EM density maps. Black – gold-standard Fourier shell correlation (FSC) curves, showing the overall nominal resolutions of 3.26 Å at 0.143 criterion; gray – Map-model FSC plot calculated by Phenix. **c**, Cryo-EM map colored based on local resolution. **d**, Focused 3D refined ARM2 map colored based on local resolution. **e**, Resolution estimation of the focused 3D refined ARM2 domain density map. Black – gold-standard Fourier shell correlation (FSC) curves, showing the overall nominal resolutions of 3.6 Å at 0.143 criterion; gray - Map-model FSC plot calculated by Phenix.

Extended Data Figure 3. Cryo-EM processing workflow for CIA-IP_3R1.

Extended Data Figure 4. Characteristics of cryo-EM reconstructions for CIA-IP_3R1. **a,** Euler angle distribution of particles contributing to the final reconstruction with larger red cylinders representing orientations comprising more particles. **b,** Resolution estimation of the cryo-EM density maps. Black – gold-standard Fourier shell correlation (FSC) curves, showing the overall nominal resolutions of 3.5 Å at 0.143 criterion; blue - Map-model FSC plot calculated by Phenix. **c,** Cryo-EM map colored based on local resolution. **d,** Focused 3D refined ARM2 map colored based on local resolution. **e**, Resolution estimation of the focused 3D refined ARM2 domain density map. Black – gold-standard Fourier shell correlation (FSC) curves, showing the overall nominal resolutions of 3.7 Å at 0.143 criterion; blue - Map-model FSC plot calculated by Phenix.

Extended Data Figure 5. 3D focused classification and local refinement on ARM2 domain for Apo-IP_3R1 in nanodisc used in Baker et al.[27]

Extended Data Figure 6. Atomic models for the full-length tetrameric assembly of CIA-IP_3R1 (a) and Ca-IP_3R1 (b) based on the respective cryo-EM density maps. Top panels show a side view along the membrane plane. Transmembrane boundaries are indicated in gray. Bottom panels show a top-view from the cytosol along the four-fold axis. **b**, Cα RMS deviations were calculated between CIA-IP_3R1 and Ca-IP_3R1 (**c**) and Ca-IP_3R1 and apo-IP_3R1 (PDB ID: 7LHE) (**d**) resulting in 11 Å and 2 Å RMSD, respectively. Per-residue deviations are mapped onto one subunit from CIA-IP_3R1 (top panel) and Ca-IP_3R1 (bottom panel) and color-coded based on their deviation lowest RMSD (blue/thinnest) to highest RMSD (red/thickest) is reflected in the ribbon color/thickness.

Extended Data Figure 7. Structural features in the IP_3R1 transmembrane domains. a, Densities (gray) for TMDs TM4 through TM6 from one subunit are overlaid with their atomic models CIA-IP_3R1 (blue-green), Ca-IP_3R1 (pink) and membrane boundaries indicated. **b,** Non-protein densities (gray mesh) within the transmembrane domains corresponding to lipids were identified in CIA-IP_3R1 (left) and Ca-IP_3R1 (right) are consistent with those described in Baker et al.[27]. The model of the TMDs is depicted as a ribbon and viewed parallel to the membrane plane. Lipids are represented as ball-and-stick models and labeled L1–L7. **c,** TM6 helix in CIA-IP_3R1 (blue-green) is overlaid with cryo-EM densities, colored gray (oxygen atoms - red; nitrogen atoms - blue; sulfur atoms - yellow). Boxed region indicates the location for the π-helix in TM6 and zoomed in on the right panels (CIA-IP_3R1 (blue-green), Ca-IP_3R1 (pink).

Extended Data Figure 8. Properties within the IP_3 and ATP ligand binding pockets. a, Schematic plot of the IP_3 molecule interacting with surrounding residues within the in CIA-IP_3R1 structure. **b,** Schematic plot of the Adenophostin A molecule interacting with surrounding residues in the ADA-IP_3R1 (PDB ID: 6MU1) structure. IP_3R1 residues that are consistent in coordinating ADA and IP_3 are underlined. Arcs represent hydrophobic interactions, green dashed lines are H-bonds as calculated in LigPlot+[93]. **c,** Structural alignment and overlay of the IP_3 binding pocket in CIA-IP_3R1 (blue-green) and ADA-IP_3R1 (PDB ID: 6MU1, white). **d**, Coulombic electrostatic potential calculated and displayed on the surface representation of the IP_3 binding pocket in CIA-IP_3R1 with the pocket lining residues labeled. Blue indicates positive, red indicates positive. **e**, Coulombic electrostatic potential calculated and displayed on the surface representation of the ATP binding pocket in CIA-IP_3R1 with the pocket lining residues labeled. Zoomed-in view of the ATP binding pocket in apo-IP_3R1 (EMDB: 23337) overlaid with its molecular model (PBD ID: 7LHE) and focused on the side chain conformers for W2639.

Extended Data Figure 9. Ca^{2+} binding sites found in CIA-IP_3R1. Ca^{2+} binding sites in the CIA-IP_3R1 localized in the ligand binding domain (Ca-II_{LBD}), Ca^{2+} sensor in ARM3 domain (Ca-III_s), and luminal vestibule of the TMD (Ca-IV_L and Ca-V_L). Ca^{2+} ions are shown as green spheres and overlaid with corresponding densities displayed at 2-5 σ cutoff values. Residues within 5 Å of the Ca^{2+} ions are displayed in a stick representation and labeled.

Extended Data Video 1. Three-dimensional variability analysis shows flexibility of CIA-IP_3R1 exhibits dynamic motions involving both the cytoplasmic and pore domains

Extended Data Video 2. Three-dimensional variability analysis shows motion dynamics of CIA-IP_3R1 in nexus region.

Extended Data Video 3. Three-dimensional variability analysis shows motion dynamics of CIA-IP_3R1 in cytoplasmic domain, particularly ARM2 domain.

References

1. Bezprozvanny, I. & Hayden, M. R. Deranged neuronal calcium signaling and Huntington disease. Biochem Biophys Res Commun. 2004;322(4):1310-1317. Epub 2004/09/01. doi: 10.1016/j.bbrc.2004.08.035. PMID: 15336977.
2. Bezprozvanny, I. *Inositol 1,4,5-tripshosphate receptor, calcium signalling and Huntington's disease*. Vol. 45 (Springer, 2007).
3. Foskett, J. K. Inositol trisphosphate receptor Ca^{2+} release channels in neurological diseases. Pflugers Arch. 2010;460(2):481-494. Epub 2010/04/13. doi: 10.1007/s00424-010-0826-0. PMID: 20383523; PMCID: PMCPMC2893360.
4. Bezprozvanny, I. Role of inositol 1,4,5-trisphosphate receptors in pathogenesis of Huntington's disease and spinocerebellar ataxias. Neurochemical research. 2011;36(7):1186-1197. Epub 2011/01/07. doi: 10.1007/s11064-010-0393-y. PMID: 21210219; PMCID: PMCPMC3094593.
5. Hisatsune, C. & Mikoshiba, K. IP3 receptor mutations and brain diseases in human and rodents. J Neurochem. 2017;141(6):790-807. Epub 2017/02/18. doi: 10.1111/jnc.13991. PMID: 28211945.
6. Huang, L., Chardon, J. W., Carter, M. T., Friend, K. L., Dudding, T. E. *et al.* Missense mutations in ITPR1 cause autosomal dominant congenital nonprogressive spinocerebellar ataxia. Orphanet J Rare Dis. 2012;7:67. Epub 2012/09/19. doi: 10.1186/1750-1172-7-67. PMID: 22986007; PMCID: PMCPMC3545966.
7. Foskett, J. K., White, C., Cheung, K. H. & Mak, D. O. Inositol trisphosphate receptor Ca2+ release channels. Physiol Rev. 2007;87(2):593-658. PMID: 17429043.
8. Prole, D. L. & Taylor, C. W. Inositol 1,4,5-trisphosphate receptors and their protein partners as signalling hubs. J Physiol. 2016. doi: 10.1113/JP271139. PMID: 26830355.
9. Alzayady, K. J., Wang, L., Chandrasekhar, R., Wagner, L. E., 2nd, Van Petegem, F. *et al.* Defining the stoichiometry of inositol 1,4,5-trisphosphate binding required to initiate Ca^{2+} release. Science signaling. 2016;9(422):ra35. doi: 10.1126/scisignal.aad6281. PMID: 27048566; PMCID: PMC4850551.
10. Bosanac, I., Michikawa, T., Mikoshiba, K. & Ikura, M. Structural insights into the regulatory mechanism of IP3 receptor. Biochim Biophys Acta. 2004;1742(1-3):89-102. PMID: 15590059.
11. Bezprozvanny, I., Watras, J. & Ehrlich, B. E. Bell-shaped calcium-response curves of Ins(1,4,5)P3- and calcium-gated channels from endoplasmic reticulum of cerebellum. Nature. 1991;351(6329):751-754. PMID: 1648178.
12. Mak, D. O., McBride, S. & Foskett, J. K. Atp regulation of recombinant type 3 inositol 1,4,5-trisphosphate receptor gating. J Gen Physiol. 2001;117(5):447-456. PMID: 11331355.
13. Foskett, J. K. & Daniel Mak, D. O. Regulation of IP(3)R Channel Gating by Ca^{2+} and Ca^{2+} Binding Proteins. Current topics in membranes. 2010;66:235-272. Epub 2010/01/01. doi: 10.1016/S1063-5823(10)66011-5. PMID: 22353483; PMCID: PMCPMC6707373.
14. Betzenhauser, M. J., Wagner, L. E., 2nd, Iwai, M., Michikawa, T., Mikoshiba, K. *et al.* ATP modulation of Ca^{2+} release by type-2 and type-3 inositol (1, 4, 5)-triphosphate receptors. Differing ATP sensitivities and molecular determinants of action. J Biol Chem. 2008;283(31):21579-21587. PMID: 18505727.

15. Mak, D. O., McBride, S. & Foskett, J. K. ATP-dependent Adenophostin Activation of Inositol 1,4,5-Trisphosphate Receptor Channel Gating. Kinetic implications for the durations of calcium puffs in cells. J Gen Physiol. 2001;117(4):299-314. PMID: 11279251.
16. Mak, D. O., McBride, S. & Foskett, J. K. Regulation by Ca^{2+} and Inositol 1,4,5-Trisphosphate InsP3 of Single Recombinant Type 3 InsP3 Receptor Channels. Ca^{2+} activation uniquely distinguishes types 1 and 3 InsP3 receptors. J Gen Physiol. 2001;117(5):435-446. PMID: 11331354.
17. Mak, D. O., McBride, S. & Foskett, J. K. ATP regulation of type 1 inositol 1,4,5-trisphosphate receptor channel gating by allosteric tuning of Ca^{2+} activation. J Biol Chem. 1999;274(32):22231-22237. PMID: 10428789.
18. Hagar, R. E. & Ehrlich, B. E. Regulation of the type III InsP3 receptor by InsP3 and ATP. Biophys J. 2000;79(1):271-278. PMID: 10866953.
19. Betzenhauser, M. J., Wagner, L. E., 2nd, Park, H. S. & Yule, D. I. ATP regulation of type-1 inositol 1,4,5-trisphosphate receptor activity does not require walker A-type ATP-binding motifs. J Biol Chem. 2009;284(24):16156-16163. doi: 10.1074/jbc.M109.006452. PMID: 19386591; PMCID: PMC2713511.
20. Wagner, L. E., 2nd & Yule, D. I. Differential regulation of the InsP(3) receptor type-1 and -2 single channel properties by InsP3, Ca^{2+} and ATP. J Physiol. 2012;590(Pt 14):3245-3259. doi: 10.1113/jphysiol.2012.228320. PMID: 22547632; PMCID: PMC3459040.
21. Bezprozvanny, I. & Ehrlich, B. E. ATP modulates the function of inositol 1,4,5-trisphosphate-gated channels at two sites. Neuron. 1993;10(6):1175-1184. PMID: 7686381.
22. Tu, H., Wang, Z., Nosyreva, E., De Smedt, H. & Bezprozvanny, I. Functional characterization of mammalian inositol 1,4,5-trisphosphate receptor isoforms. Biophys J. 2005;88(2):1046-1055. PMID: 15533917.
23. Fan, G., Baker, M. L., Wang, Z., Baker, M. R., Sinyagovskiy, P. A. *et al.* Gating machinery of InsP3R channels revealed by electron cryomicroscopy. Nature. 2015;527(7578):336-341. doi: 10.1038/nature15249. PMID: 26458101; PMCID: PMC4804758.
24. Fan, G., Baker, M. R., Wang, Z., Seryshev, A. B., Ludtke, S. J. *et al.* Cryo-EM reveals ligand induced allostery underlying InsP3R channel gating. Cell research. 2018;28(12):1158-1170. doi: 10.1038/s41422-018-0108-5. PMID: 30470765; PMCID: PMC6274648.
25. Paknejad, N. & Hite, R. K. Structural basis for the regulation of inositol trisphosphate receptors by Ca(2+) and IP3. Nat Struct Mol Biol. 2018;25(8):660-668. doi: 10.1038/s41594-018-0089-6. PMID: 30013099; PMCID: PMC6082148.
26. Azumaya, C. M., Linton, E. A., Risener, C. J., Nakagawa, T. & Karakas, E. Cryo-EM structure of human type-3 inositol triphosphate receptor reveals the presence of a self-binding peptide that acts as an antagonist. J Biol Chem. 2020;295(6):1743-1753. Epub 2020/01/10. doi: 10.1074/jbc.RA119.011570. PMID: 31915246; PMCID: PMCPMC7008357.
27. Baker, M. R., Fan, G., Seryshev, A. B., Agosto, M. A., Baker, M. L. *et al.* Cryo-EM structure of type 1 IP3R channel in a lipid bilayer. Commun Biol. 2021;4(1):625. Epub 2021/05/27. doi: 10.1038/s42003-021-02156-4. PMID: 34035440; PMCID: PMCPMC8149723.
28. Schmitz, E. A., Takahashi, H. & Karakas, E. Structural basis for activation and gating of IP3 receptors. Nature communications. 2022;13(1):1408. Epub 2022/03/19. doi: 10.1038/s41467-022-29073-2. PMID: 35301323.
29. Chen, M. & Ludtke, S. J. Deep learning-based mixed-dimensional Gaussian mixture model for characterizing variability in cryo-EM. Nature methods. 2021;18(8):930-936.

Epub 2021/07/31. doi: 10.1038/s41592-021-01220-5. PMID: 34326541; PMCID: PMCPMC8363932.

30. Arige, V., Terry, L. E., Wagner, L. E., 2nd, Baker, M. R., Fan, G. *et al.* Functional Determination of Calcium Binding Sites Required for the Activation of Inositol 1,4,5-trisphosphate receptors. bioRxiv 482538. 2022. doi: https://doi.org/10.1101/2022.03.07.482538.
31. Mak, D.-O., McBride, S. & Foskett, J. K. Inositol 1,4,5-triphosphate activation of inositol triphosphate receptor Ca^{2+} channel by ligand tuning of Ca^{2+} inhibition. Proc. Natl. Acad. Sci. USA. 1998;95:15821-15825.
32. Mak, D. O., McBride, S. M., Petrenko, N. B. & Foskett, J. K. Novel regulation of calcium inhibition of the inositol 1,4,5-trisphosphate receptor calcium-release channel. J Gen Physiol. 2003;122(5):569-581. PMID: 14581583.
33. Ferris, C. D., Huganir, R. L. & Snyder, S. H. Calcium flux mediated by purified inositol 1,4,5-trisphosphate receptor in reconstituted lipid vesicles is allosterically regulated by adenine nucleotides. Proc Natl Acad Sci U S A. 1990;87(6):2147-2151. PMID: 2156262.
34. Maeda, N., Kawasaki, T., Nakade, S., Yokota, N., Taguchi, T. *et al.* Structural and functional characterization of inositol 1,4,5- trisphosphate receptor channel from mouse cerebellum. J Biol Chem. 1991;266(2):1109-1116. PMID: 1845986.
35. Supattapone, S., Worley, P. F., Baraban, J. M. & Snyder, S. H. Solubilization, purification and characteriztion of an inositol triphosphate receptor. J Biol Chem. 1988;263:1530-1534.
36. Maeda, N., Niinobe, M. & Mikoshiba, K. A cerebellar Purkinje cell marker P_{400} protein is an inositol 1,4,5-triphosphate ($insP_3$) receptor protein. Purification and characterization of $InsP_3$ receptor complex. Embo J. 1990;9(1):61-67.
37. Kaftan, E. J., Ehrlich, B. E. & Watras, J. Inositol 1,4,5-triphosphate ($InsP_3$) and calcium interact to increase the dynamic range of $InsP_3$ receptor-dependent calcium signaling. J Gen Physiol. 1997;110:529-538.
38. Ramos-Franco, J., Caenepeel, S., Fill, M. & Mignery, G. Single channel function of recombinant type-1 inositol 1,4,5- trisphosphate receptor ligand binding domain splice variants. Biophys J. 1998;75(6):2783-2793. PMID: 9826600.
39. Ramos-Franco, J., Fill, M. & Mignery, G. A. Isoform-specific function of single inositol 1,4,5-trisphosphate receptor channels. Biophys J. 1998;75(2):834-839.
40. Striggow, F. & Ehrlich, B. E. The inositol 1,4,5-trisphosphate receptor of cerebellum. Mn^{2+} permeability and regulation by cytosolic Mn^{2+}. J Gen Physiol. 1996;108(2):115-124. PMID: 8854341.
41. Tu, H., Miyakawa, T., Wang, Z., Glouchankova, L., Iino, M. *et al.* Functional characterization of the type 1 inositol 1,4,5-trisphosphate receptor coupling domain SII(+/-) splice variants and the Opisthotonos mutant form. Biophys J. 2002;82(4):1995-2004. PMID: 11916857.
42. Bosanac, I., Alattia, J. R., Mal, T. K., Chan, J., Talarico, S. *et al.* Structure of the inositol 1,4,5-trisphosphate receptor binding core in complex with its ligand. Nature. 2002;420(6916):696-700. PMID: 12442173.
43. Bosanac, I., Yamazaki, H., Matsu-Ura, T., Michikawa, T., Mikoshiba, K. *et al.* Crystal structure of the ligand binding suppressor domain of type 1 inositol 1,4,5-trisphosphate receptor. Mol Cell. 2005;17(2):193-203. PMID: 15664189.
44. Ludtke, S. J., Tran, T. P., Ngo, Q. T., Moiseenkova-Bell, V. Y., Chiu, W. *et al.* Flexible architecture of IP3R1 by Cryo-EM. Structure. 2011;19(8):1192-1199. doi: 10.1016/j.str.2011.05.003. PMID: 21827954; PMCID: PMC3154621.
45. Lin, C. C., Baek, K. & Lu, Z. Apo and InsP-bound crystal structures of the ligand-binding domain of an InsP receptor. Nat Struct Mol Biol. 2011;18(10):1172-1174. PMID: 21892169.

46. Seo, M. D., Velamakanni, S., Ishiyama, N., Stathopulos, P. B., Rossi, A. M. *et al.* Structural and functional conservation of key domains in InsP3 and ryanodine receptors. Nature. 2012;483(7387):108-112. Epub 2012/01/31. doi: 10.1038/nature10751. PMID: 22286060; PMCID: PMC3378505.
47. Wilcox, R. A., Primrose, W. U., Nahorski, S. R. & Challiss, R. A. New developments in the molecular pharmacology of the myo-inositol 1,4,5-trisphosphate receptor. Trends Pharmacol Sci. 1998;19(11):467-475. Epub 1998/12/16. doi: 10.1016/s0165-6147(98)01260-7. PMID: 9850611.
48. Kozikowski, A. P., Ognyanov, V. I., Chen, C., Fauq, A. H., Safrany, S. T. *et al.* Deoxygenated inositol 1,4,5-trisphosphate analogues and their interaction with metabolic enzymes. (1R,2R,4R)-cyclohexane-1,2,4-tris(methylenesulfonate): a potent selective 5-phosphatase inhibitor. Journal of medicinal chemistry. 1993;36(20):3035-3038. Epub 1993/10/01. doi: 10.1021/jm00072a027. PMID: 8411022.
49. Hamada, K., Miyatake, H., Terauchi, A. & Mikoshiba, K. IP3-mediated gating mechanism of the IP3 receptor revealed by mutagenesis and X-ray crystallography. Proc Natl Acad Sci U S A. 2017;114(18):4661-4666. doi: 10.1073/pnas.1701420114. PMID: 28416699; PMCID: PMC5422816.
50. Yoshikawa, F., Morita, M., Monkawa, T., Michikawa, T., Furuichi, T. *et al.* Mutational analysis of the ligand binding site of the inositol 1,4,5- trisphosphate receptor. J Biol Chem. 1996;271(30):18277-18284. PMID: 8663526.
51. Swatton, J. E., Morris, S. A., Cardy, T. J. & Taylor, C. W. Type 3 inositol trisphosphate receptors in RINm5F cells are biphasically regulated by cytosolic Ca^{2+} and mediate quantal Ca^{2+} mobilization. Biochem J. 1999;344 Pt 1:55-60. PMID: 10548533.
52. Marchant, J. S. & Taylor, C. W. Cooperative activation of IP_3 receptors by sequential binding of IP_3 and Ca^{2+} safeguards against spontaneous activity. Curr Biol. 1997;7(7):510-518. PMID: 9210378.
53. Adkins, C. E. & Taylor, C. W. Lateral inhibition of inositol 1,4,5-trisphosphate receptors by cytosolic Ca^{2+}. Curr Biol. 1999;9(19):1115-1118. PMID: 10531009.
54. Sienaert, I., Nadif Kasri, N., Vanlingen, S., Parys, J. B., Callewaert, G. *et al.* Localization and function of a calmodulin-apocalmodulin-binding domain in the N-terminal part of the type 1 inositol 1,4,5-trisphosphate receptor. Biochem J. 2002;365(Pt 1):269-277. PMID: 11955285.
55. Baker, M. R., Fan, G. & Serysheva, II. Structure of IP_3R channel: high-resolution insights from cryo-EM. Current opinion in structural biology. 2017;46:38-47. doi: 10.1016/j.sbi.2017.05.014. PMID: 28618351.
56. Du, G. G. & MacLennan, D. H. Functional consequences of mutations of conserved, polar amino acids in transmembrane sequences of the Ca^{2+} release channel (ryanodine receptor) of rabbit skeletal muscle sarcoplasmic reticulum. J Biol Chem. 1998;273(48):31867-31872. PMID: 9822655.
57. Miyakawa, T., Mizushima, A., Hirose, K., Yamazawa, T., Bezprozvanny, I. *et al.* Ca^{2+}-sensor region of IP_3 receptor controls intracellular Ca^{2+} signaling. Embo J. 2001;20(7):1674-1680. PMID: 11285231.
58. Terry, L. E., Alzayady, K. J., Furati, E. & Yule, D. I. Inositol 1,4,5-trisphosphate Receptor Mutations associated with Human Disease. Messenger (Los Angel). 2018;6(1-2):29-44. Epub 2018/09/11. PMID: 30197841; PMCID: PMCPMC6128530.
59. Maes, K., Missiaen, L., Parys, J. B., De Smet, P., Sienaert, I. *et al.* Mapping of the atp-binding sites on inositol 1,4,5-trisphosphate receptor type 1 and type 3 homotetramers by controlled proteolysis and photoaffinity labeling. J Biol Chem. 2001;276(5):3492-3497. PMID: 11035010.
60. Wierenga, R. K. & Hol, W. G. Predicted nucleotide-binding properties of p21 protein and its cancer-associated variant. Nature. 1983;302(5911):842-844. PMID: 6843652.

61. Fulton, J., Heald, S., Badayl, Y. & Simonson, J. Understanding the Effects of Concentration on the Solvation Structure of Ca^{2+} in Aqueous Solution. I: The Perspective on Local Structure from EXAFS and XANES. J Phys Chem. 2003;107:4688-4696.
62. Tang, L., Gamal El-Din, T. M., Payandeh, J., Martinez, G. Q., Heard, T. M. *et al.* Structural basis for Ca2+ selectivity of a voltage-gated calcium channel. Nature. 2014;505(7481):56-61. doi: 10.1038/nature12775. PMID: 24270805; PMCID: PMC3877713.
63. Hayashi, S., Uehara, D. T., Tanimoto, K., Mizuno, S., Chinen, Y. *et al.* Comprehensive investigation of CASK mutations and other genetic etiologies in 41 patients with intellectual disability and microcephaly with pontine and cerebellar hypoplasia (MICPCH). PloS one. 2017;12(8):e0181791. Epub 2017/08/08. doi: 10.1371/journal.pone.0181791. PMID: 28783747; PMCID: PMCPMC5546575.
64. Zambonin, J. L., Bellomo, A., Ben-Pazi, H., Everman, D. B., Frazer, L. M. *et al.* Spinocerebellar ataxia type 29 due to mutations in ITPR1: a case series and review of this emerging congenital ataxia. Orphanet J Rare Dis. 2017;12(1):121. Epub 2017/07/01. doi: 10.1186/s13023-017-0672-7. PMID: 28659154; PMCID: PMCPMC5490223.
65. Ionescu, L., Cheung, K. H., Vais, H., Mak, D. O., White, C. *et al.* Graded recruitment and inactivation of single InsP3 receptor Ca^{2+}-release channels: implications for quantal [corrected] Ca^{2+}release. J Physiol. 2006;573(Pt 3):645-662. PMID: 16644799.
66. Ionescu, L., White, C., Cheung, K. H., Shuai, J., Parker, I. *et al.* Mode switching is the major mechanism of ligand regulation of InsP3 receptor calcium release channels. J Gen Physiol. 2007;130(6):631-645. doi: 10.1085/jgp.200709859. PMID: 17998395; PMCID: PMC2151663.
67. Rosales, R. A., Fill, M. & Escobar, A. L. Calcium regulation of single ryanodine receptor channel gating analyzed using HMM/MCMC statistical methods. J Gen Physiol. 2004;123(5):533-553. Epub 2004/04/28. doi: 10.1085/jgp.200308868. PMID: 15111644; PMCID: PMCPMC2234502.
68. Zahradnikova, A., Dura, M. & Gyorke, S. Modal gating transitions in cardiac ryanodine receptors during increases of Ca^{2+} concentration produced by photolysis of caged Ca^{2+}. Pflugers Arch. 1999;438(3):283-288. Epub 1999/07/10. doi: 10.1007/s004240050911. PMID: 10398857.
69. Milone, M., Wang, H. L., Ohno, K., Prince, R., Fukudome, T. *et al.* Mode switching kinetics produced by a naturally occurring mutation in the cytoplasmic loop of the human acetylcholine receptor epsilon subunit. Neuron. 1998;20(3):575-588. Epub 1998/04/16. doi: 10.1016/s0896-6273(00)80996-4. PMID: 9539130.
70. Chakrapani, S., Cordero-Morales, J. F., Jogini, V., Pan, A. C., Cortes, D. M. *et al.* On the structural basis of modal gating behavior in K^+ channels. Nat Struct Mol Biol. 2011;18(1):67-74. PMID: 21186363.
71. Popescu, G., Robert, A., Howe, J. R. & Auerbach, A. Reaction mechanism determines NMDA receptor response to repetitive stimulation. Nature. 2004;430(7001):790-793. Epub 2004/08/13. doi: 10.1038/nature02775. PMID: 15306812.
72. Rothberg, B. S., Bello, R. A., Song, L. & Magleby, K. L. High Ca^{2+} concentrations induce a low activity mode and reveal Ca^{2+}-independent long shut intervals in BK channels from rat muscle. J Physiol. 1996;493 (Pt 3):673-689. Epub 1996/06/15. doi: 10.1113/jphysiol.1996.sp021414. PMID: 8799891; PMCID: PMCPMC1159017.
73. Park, E. & MacKinnon, R. Structure of the CLC-1 chloride channel from Homo sapiens. eLife. 2018;7. Epub 2018/05/29. doi: 10.7554/eLife.36629. PMID: 29809153; PMCID: PMCPMC6019066.
74. Sun, J. & MacKinnon, R. Structural Basis of Human KCNQ1 Modulation and Gating. Cell. 2020;180(2):340-347 e349. Epub 2019/12/31. doi: 10.1016/j.cell.2019.12.003. PMID: 31883792; PMCID: PMCPMC7083075.

75. Zhao, C. & MacKinnon, R. Molecular structure of an open human KATP channel. Proc Natl Acad Sci U S A. 2021;118(48). Epub 2021/11/25. doi: 10.1073/pnas.2112267118. PMID: 34815345; PMCID: PMCPMC8640745.
76. Lee, C. H. & MacKinnon, R. Activation mechanism of a human SK-calmodulin channel complex elucidated by cryo-EM structures. Science. 2018;360(6388):508-513. Epub 2018/05/05. doi: 10.1126/science.aas9466. PMID: 29724949; PMCID: PMCPMC6241251.
77. Hansen, S. B., Tao, X. & MacKinnon, R. Structural basis of PIP2 activation of the classical inward rectifier K^+ channel Kir2.2. Nature. 2011;477(7365):495-498. Epub 2011/08/30. doi: 10.1038/nature10370. PMID: 21874019; PMCID: PMCPMC3324908.
78. Whorton, M. R. & MacKinnon, R. X-ray structure of the mammalian GIRK2-betagamma G-protein complex. Nature. 2013;498(7453):190-197. Epub 2013/06/07. doi: 10.1038/nature12241. PMID: 23739333; PMCID: PMCPMC4654628.
79. Park, H. S., Betzenhauser, M. J., Won, J. H., Chen, J. & Yule, D. I. The type 2 inositol (1,4,5)-trisphosphate (InsP3) receptor determines the sensitivity of InsP3-induced Ca^{2+} release to ATP in pancreatic acinar cells. J Biol Chem. 2008;283(38):26081-26088. Epub 2008/07/29. doi: 10.1074/jbc.M804184200. PMID: 18658132; PMCID: PMCPMC2533790.
80. Chandrasekhar, R., Alzayady, K. J., Wagner, L. E., 2nd & Yule, D. I. Unique Regulatory Properties of Heterotetrameric Inositol 1,4,5-Trisphosphate Receptors Revealed by Studying Concatenated Receptor Constructs. J Biol Chem. 2016;291(10):4846-4860. Epub 2016/01/13. doi: 10.1074/jbc.M115.705301. PMID: 26755721; PMCID: PMCPMC4777821.
81. Zheng, S. Q., Palovcak, E., Armache, J. P., Verba, K. A., Cheng, Y. *et al.* MotionCor2: anisotropic correction of beam-induced motion for improved cryo-electron microscopy. Nature methods. 2017;14(4):331-332. Epub 2017/03/03. doi: 10.1038/nmeth.4193. PMID: 28250466; PMCID: PMCPMC5494038.
82. Bell, J. M., Chen, M., Durmaz, T., Fluty, A. C. & Ludtke, S. J. New software tools in EMAN2 inspired by EMDatabank map challenge. J Struct Biol. 2018;204(2):283-290. Epub 2018/09/07. doi: 10.1016/j.jsb.2018.09.002. PMID: 30189321; PMCID: PMCPMC6163079.
83. Zhang, K. Gctf: Real-time CTF determination and correction. J Struct Biol. 2016;193(1):1-12. Epub 2015/11/26. doi: 10.1016/j.jsb.2015.11.003. PMID: 26592709; PMCID: PMCPMC4711343.
84. Scheres, S. H. RELION: Implementation of a Bayesian approach to cryo-EM structure determination. J Struct Biol. 2012;180(3):519-530. Epub 2012/09/25. doi: 10.1016/j.jsb.2012.09.006. PMID: 23000701; PMCID: PMC3690530.
85. Rosenthal, P. B. & Henderson, R. Optimal determination of particle orientation, absolute hand, and contrast loss in single-particle electron cryomicroscopy. J Mol Biol. 2003;333(4):721-745. PMID: 14568533.
86. Kucukelbir, A., Sigworth, F. J. & Tagare, H. D. Quantifying the local resolution of cryo-EM density maps. Nature methods. 2014;11(1):63-65. doi: 10.1038/nmeth.2727. PMID: 24213166; PMCID: PMC3903095.
87. Punjani, A., Rubinstein, J. L., Fleet, D. J. & Brubaker, M. A. cryoSPARC: algorithms for rapid unsupervised cryo-EM structure determination. Nature methods. 2017;14(3):290-296. Epub 2017/02/07. doi: 10.1038/nmeth.4169. PMID: 28165473.
88. Punjani, A. & Fleet, D. J. 3D variability analysis: Resolving continuous flexibility and discrete heterogeneity from single particle cryo-EM. J Struct Biol. 2021;213(2):107702. Epub 2021/02/15. doi: 10.1016/j.jsb.2021.107702. PMID: 33582281.

89. Pettersen, E. F., Goddard, T. D., Huang, C. C., Couch, G. S., Greenblatt, D. M. *et al.* UCSF Chimera--a visualization system for exploratory research and analysis. J Comput Chem. 2004;25(13):1605-1612. PMID: 15264254.
90. Jumper, J., Evans, R., Pritzel, A., Green, T., Figurnov, M. *et al.* Highly accurate protein structure prediction with AlphaFold. Nature. 2021;596(7873):583-589. Epub 2021/07/16. doi: 10.1038/s41586-021-03819-2. PMID: 34265844; PMCID: PMCPMC8371605.
91. Krissinel, E. & Henrick, K. Inference of macromolecular assemblies from crystalline state. J Mol Biol. 2007;372(3):774-797. doi: 10.1016/j.jmb.2007.05.022. PMID: 17681537.
92. Pettersen, E. F., Goddard, T. D., Huang, C. C., Meng, E. C., Couch, G. S. *et al.* UCSF ChimeraX: Structure visualization for researchers, educators, and developers. Protein Sci. 2021;30(1):70-82. Epub 2020/09/04. doi: 10.1002/pro.3943. PMID: 32881101; PMCID: PMCPMC7737788.
93. Laskowski, R. A. & Swindells, M. B. LigPlot+: multiple ligand-protein interaction diagrams for drug discovery. Journal of chemical information and modeling. 2011;51(10):2778-2786. doi: 10.1021/ci200227u. PMID: 21919503.
94. Smart, O. S., Goodfellow, J. M. & Wallace, B. A. The pore dimensions of gramicidin A. Biophys J. 1993;65(6):2455-2460. doi: 10.1016/S0006-3495(93)81293-1. PMID: 7508762; PMCID: PMC1225986.
95. Humphrey, W., Dalke, A. & Schulten, K. VMD: visual molecular dynamics. J Mol Graph. 1996;14(1):33-38, 27-38. Epub 1996/02/01. doi: 10.1016/0263-7855(96)00018-5. PMID: 8744570.
96. Alzayady, K. J., Chandrasekhar, R. & Yule, D. I. Fragmented inositol 1,4,5-trisphosphate receptors retain tetrameric architecture and form functional Ca^{2+} release channels. J Biol Chem. 2013;288(16):11122-11134. Epub 2013/03/13. doi: 10.1074/jbc.M113.453241. PMID: 23479737; PMCID: PMC3630841.

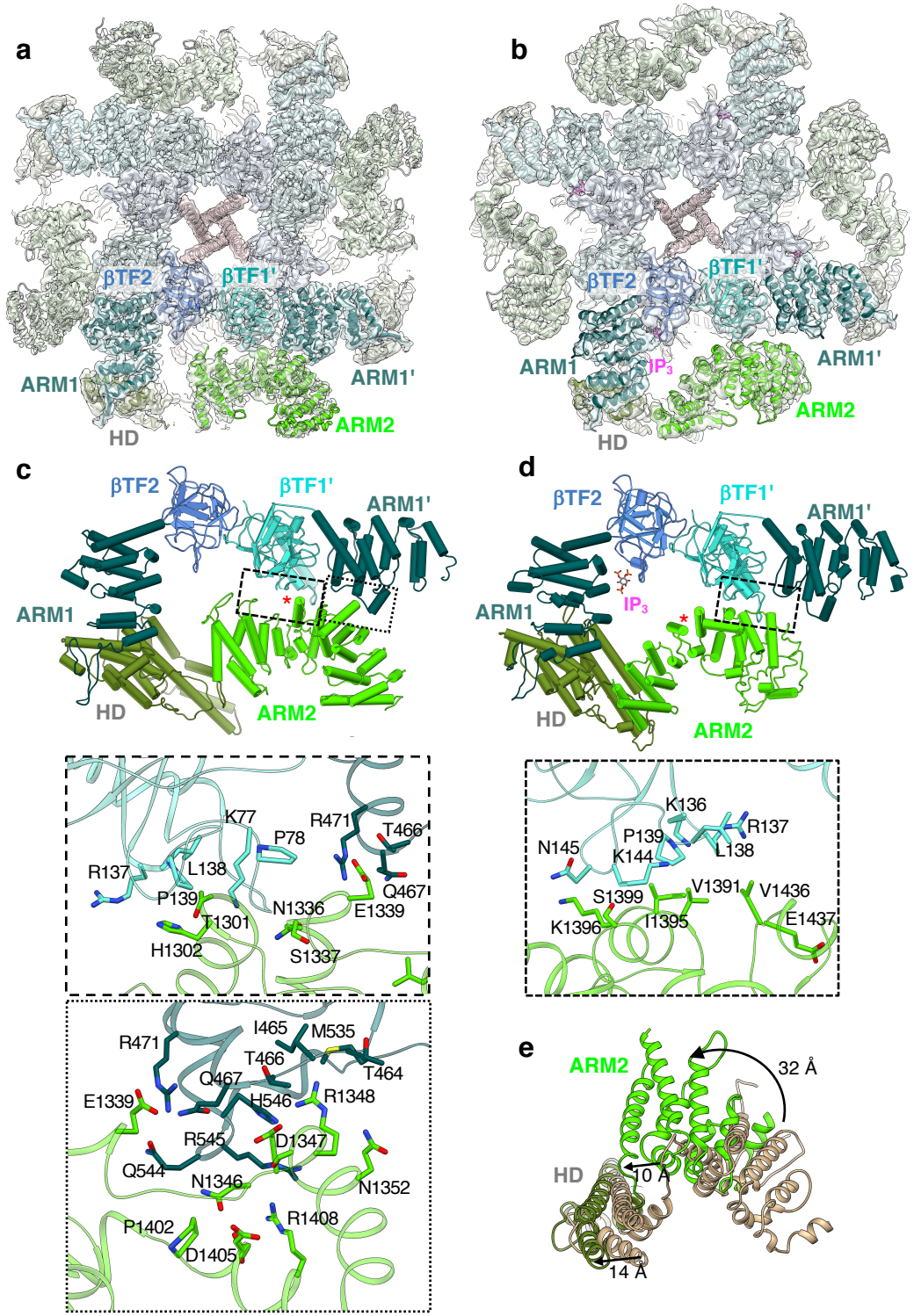
a
βTF2
βTF1'
ARM1
ARM1'
HD
ARM2
b
βTF2
βTF1'
ARM1
IP3
ARM1'
ARM2
HD
c
βTF2
βTF1'
ARM1'
ARM1
HD
ARM2
d
βTF2
βTF1'
ARM1'
IP3
ARM1
HD
ARM2
K77
P78
R471
T466
R137
L138
Q467
P139
N1336
E1339
T1301
H1302
S1337
K136
R137
N145
P139
K144
L138
S1399
V1391
V1436
K1396
I1395
E1437
R471
I465
M535
T466
T464
Q467
E1339
H546
R1348
R545
D1347
Q544
N1346
N1352
P1402
R1408
D1405
e
ARM2
32 Å
HD
10 Å
14 Å

Figure 1

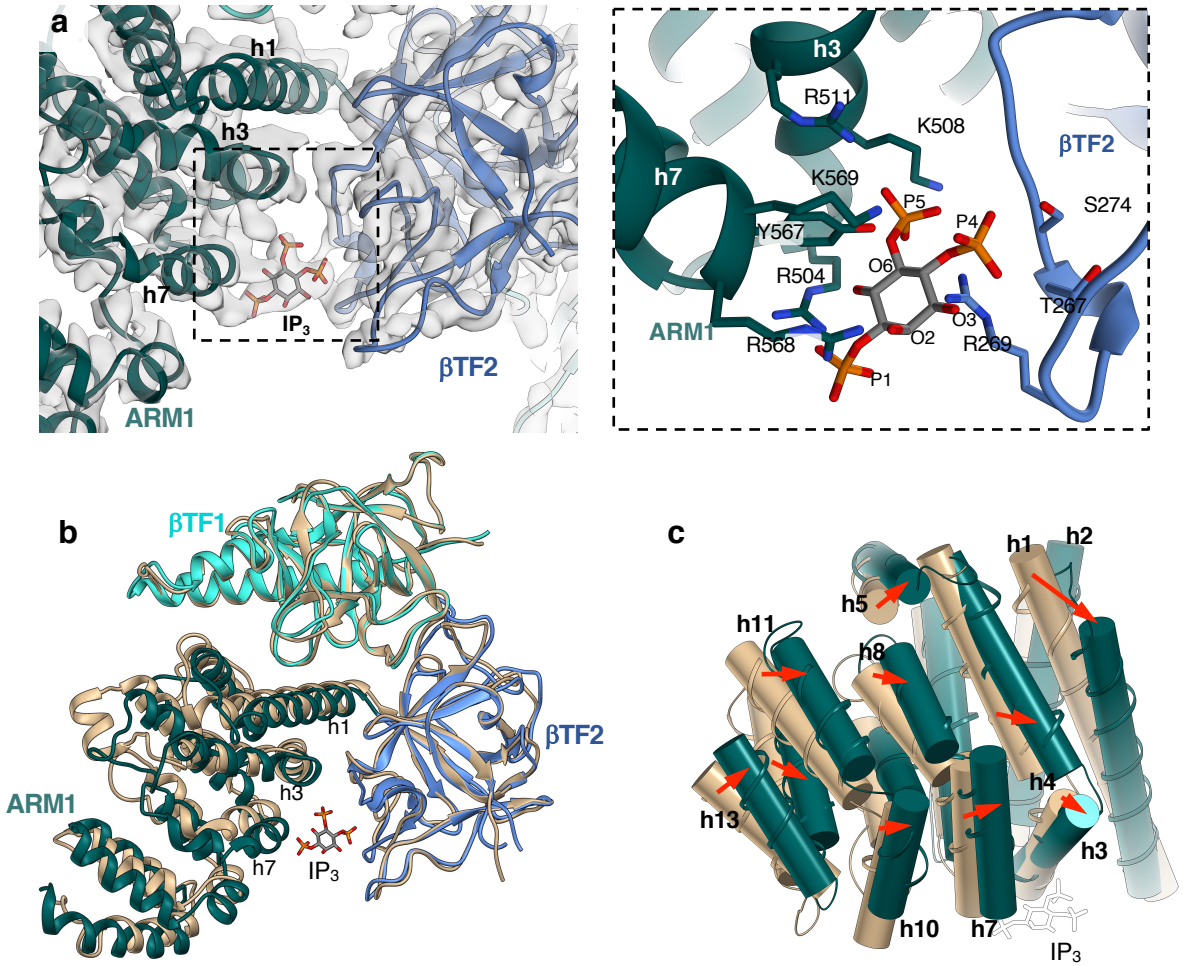
a
h1
h3
h7
IP3
βTF2
ARM1
h3
R511
K508
βTF2
h7
K569
P5
S274
Y567
P4
R504
O6
T267
ARM1
O3
R568
O2
R269
P1
b
βTF1
h1
βTF2
ARM1
h3
h7
IP3
c
h1
h2
h5
h11
h8
h4
h13
h3
h10
h7
IP3

Figure 2

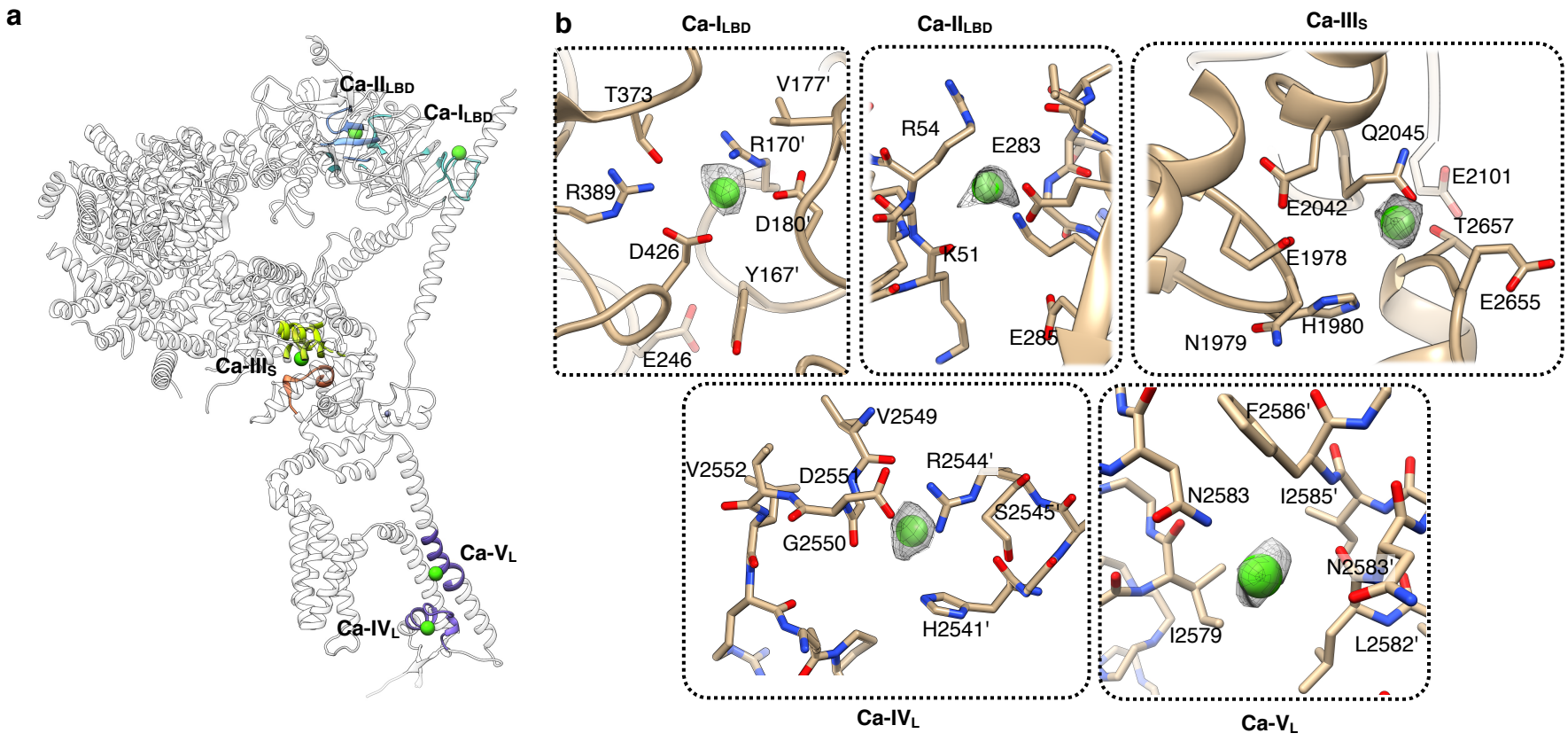
a
Ca-II$_{LBD}$
Ca-I$_{LBD}$
Ca-III$_S$
Ca-V$_L$
Ca-IV$_L$
b
Ca-I$_{LBD}$
T373
V177'
R170'
R389
D180'
D426
Y167'
E246
Ca-II$_{LBD}$
R54
E283
K51
E285
Ca-III$_S$
Q2045
E2101
E2042
T2657
E1978
E2655
H1980
N1979
V2549
V2552
D2551
R2544'
S2545'
G2550
H2541'
Ca-IV$_L$
F2586'
N2583
I2585'
N2583'
I2579
L2582'
Ca-V$_L$

Figure 3

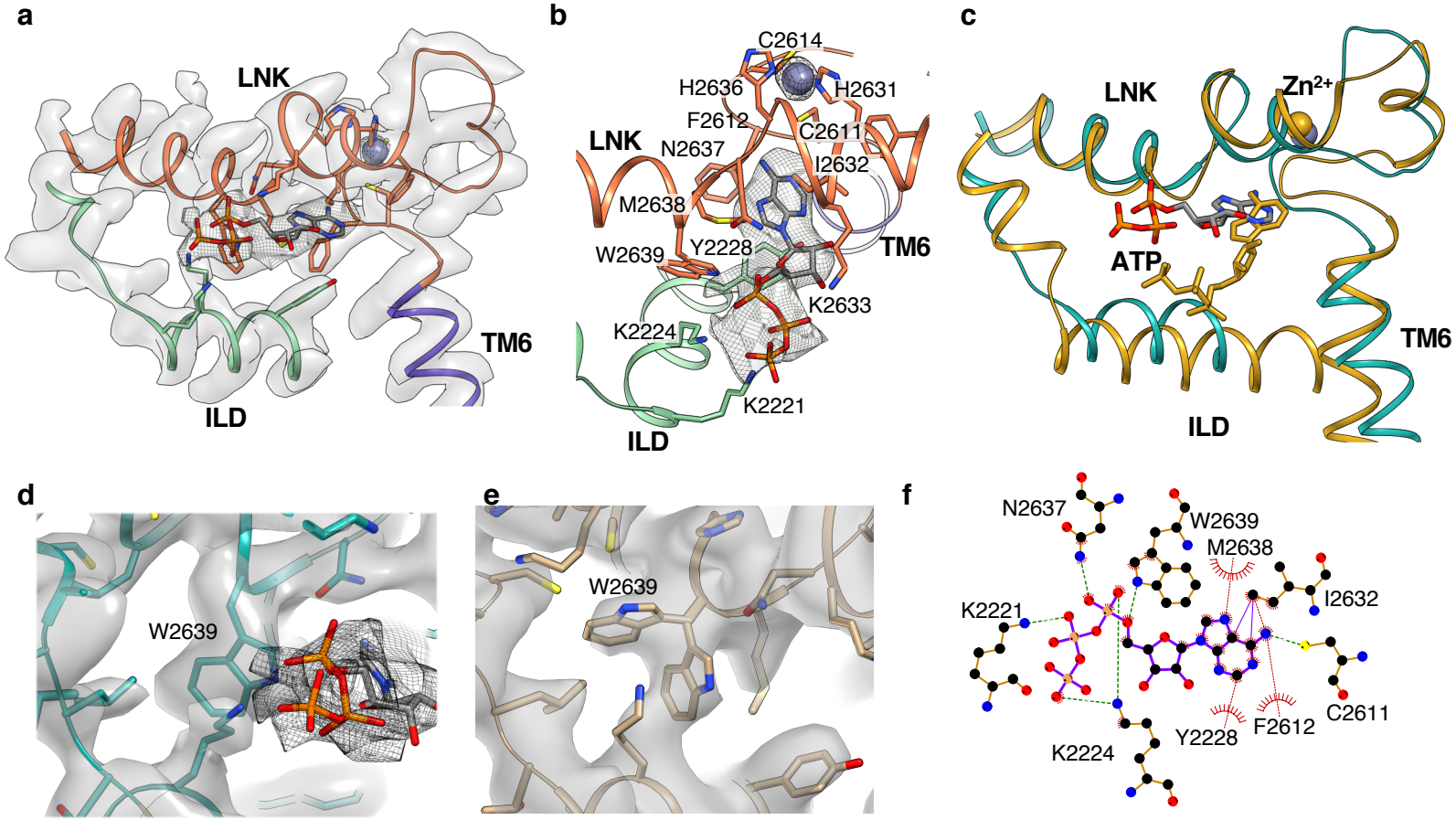
a
LNK
TM6
ILD
b
C2614
H2636
H2631
F2612
C2611
LNK
N2637
I2632
M2638
W2639
Y2228
TM6
K2633
K2224
K2221
ILD
c
LNK
Zn2+
ATP
TM6
ILD
d
W2639
e
W2639
f
N2637
W2639
M2638
I2632
K2221
C2611
F2612
Y2228
K2224

Figure 4

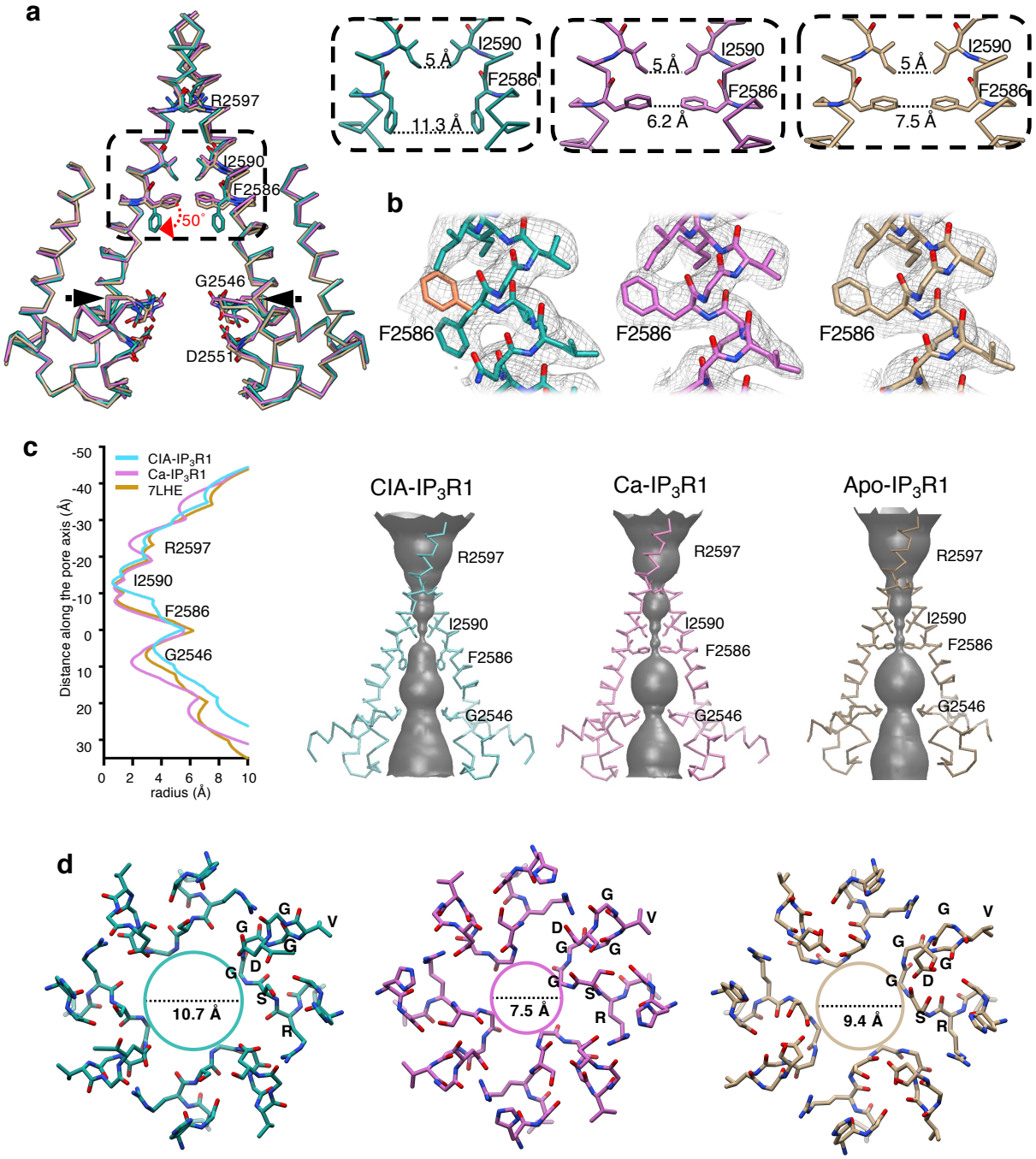
a
R2597
I2590
F2586
50°
G2546
D2551
5 Å
11.3 Å
6.2 Å
7.5 Å
b
F2586
c
CIA-IP3R1
Ca-IP3R1
7LHE
Distance along the pore axis (Å)
radius (Å)
R2597
I2590
F2586
G2546
Apo-IP3R1
d
10.7 Å
7.5 Å
9.4 Å

Figure 5

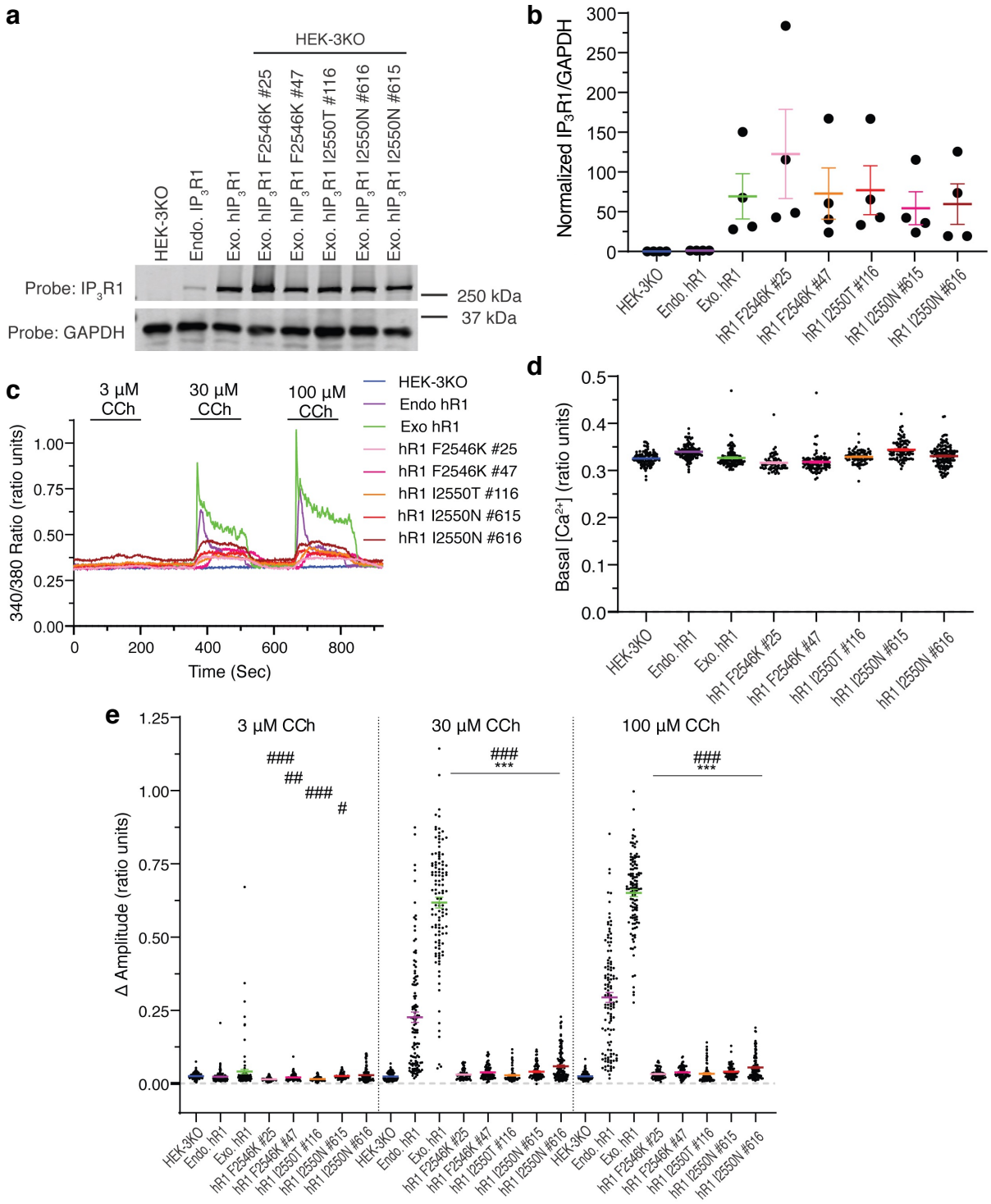
a
HEK-3KO
HEK-3KO
Endo. IP3R1
Exo. hIP3R1
Exo. hIP3R1 F2546K #25
Exo. hIP3R1 F2546K #47
Exo. hIP3R1 I2550T #116
Exo. hIP3R1 I2550N #616
Exo. hIP3R1 I2550N #615
Probe: IP3R1
Probe: GAPDH
250 kDa
37 kDa
b
Normalized IP3R1/GAPDH
c
3 μM CCh
30 μM CCh
100 μM CCh
340/380 Ratio (ratio units)
Time (Sec)
HEK-3KO
Endo hR1
Exo hR1
hR1 F2546K #25
hR1 F2546K #47
hR1 I2550T #116
hR1 I2550N #615
hR1 I2550N #616
d
Basal [Ca2+] (ratio units)
e
3 μM CCh
30 μM CCh
100 μM CCh
Δ Amplitude (ratio units)

Figure 6

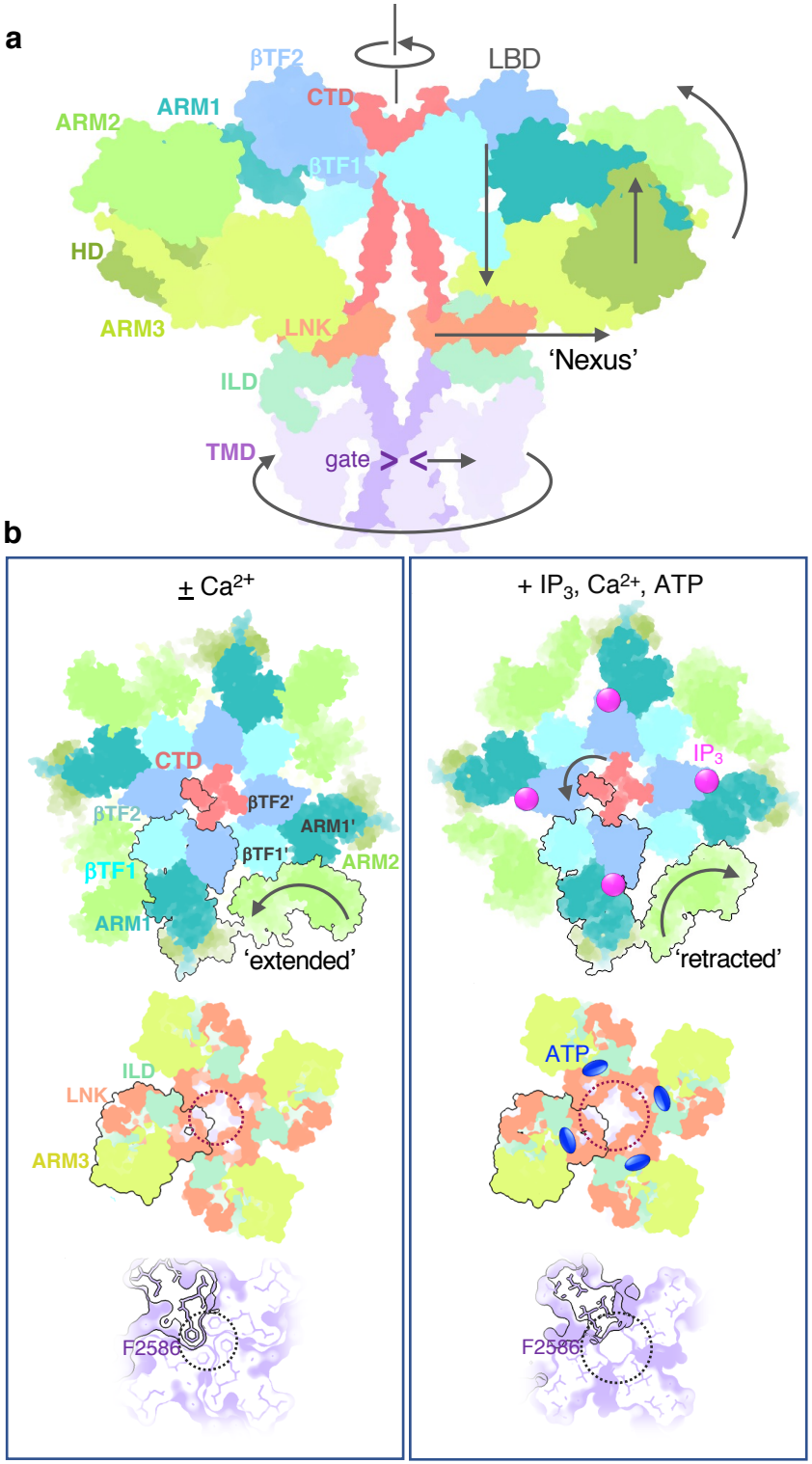
a
βTF2
LBD
CTD
ARM1
ARM2
βTF1
HD
ARM3
LNK
'Nexus'
ILD
TMD
gate
b
± Ca2+
+ IP3, Ca2+, ATP
CTD
βTF2'
βTF2
ARM1'
βTF1'
ARM2
βTF1
ARM1
'extended'
IP3
'retracted'
ILD
LNK
ARM3
ATP
F2586
F2586

Figure 7

Table 1
Cryo-EM structure determination and model statistics

	Ca-IP_3R1 (EMDB-xxxx) (PDB xxxx)	ClA-IP_3R1 (EMDB-xxxx) (PDB xxxx)
Data collection and processing		
Magnification	130k	130k
Voltage (kV)	300	300
Electron exposure (e–/Å^2)	49	49
Defocus range (μm)	-0.8 to -2.5	-0.8 to -2.5
Pixel size (Å)	1.07	1.07
Symmetry imposed	C4	C4
Initial particle images (no.)	1,855,320	1,452,797
Final particle images (no.)	346,731	133,740
Map resolution (Å)	3.26	3.50
FSC threshold	0.143	0.143
Map resolution range (Å)	2.4-6	2.4-6
Refinement		
Initial model used (PDB code)	7LHE	7LHE
Model resolution (Å) FSC=0.5	3.5	3.8
FSC threshold	0.5	0.5
Map sharpening B factor (Å^2)	-129	-157
Model composition		
Non-hydrogen atoms	77960	78516
Protein residues	9464	9552
Ligands		
IP3	NA	4
ATP	NA	4
Ca^{2+}	20	16
Zn^{2+}	4	4
lipids	28	28
B factors (Å^2)		
Protein	104.42	155.44
Ligand	72.32	123.40
R.m.s. deviations		
Bond lengths (Å)	0.003	0.003
Bond angles (°)	0.627	0.602
Validation		
MolProbity score	1.79	1.84
Clashscore	9.44	10.74
Ramachandran plot		
Favored (%)	95.86	95.78
Allowed (%)	3.97	4.05
Outliers(%)	0.17	0.17